

Astrometry meets Pulsar Timing Arrays: Synergies for Gravitational Wave Detection

N. M. Jiménez Cruz^{a 1}, Ameet Malhotra^{a 2}, Gianmassimo Tasinato^{a,b 3}, Ivonne Zavala^{a 4}

^a *Physics Department, Swansea University, SA28PP, United Kingdom*

^b *Dipartimento di Fisica e Astronomia, Università di Bologna,
INFN, Sezione di Bologna, I.S. FLAG, viale B. Pichat 6/2, 40127 Bologna, Italy*

Abstract

High-precision astrometry offers a promising approach to detect low-frequency gravitational waves, complementing pulsar timing array (PTA) observations. We explore the response of astrometric measurements to a stochastic gravitational wave background (SGWB) in synergy with PTA data. Analytical, covariant expressions for this response are derived, accounting for the presence of a possible dipolar anisotropy in the SGWB. We identify the optimal estimator for extracting SGWB information from astrometric observations and examine how sensitivity to SGWB properties varies with the sky positions of stars and pulsars. Using representative examples of current PTA capabilities and near-future astrometric sensitivity, we demonstrate that cross-correlating astrometric and PTA data can improve constraints on SGWB properties, compared to PTA data alone. The improvement is quantified through Fisher forecasts for the SGWB amplitude, spectral tilt, and dipolar anisotropy amplitude. In the future, such joint constraints could play a crucial role in identifying the origin of SGWB signals detected by PTAs.

1 Introduction

The detection of a stochastic background of gravitational waves (SGWB) would represent a major milestone for gravitational wave astronomy. Recent exciting developments in the nano-Hertz (nHz) frequency regime suggest that we may be on the verge of a detection, with several Pulsar Timing Array (PTA) collaborations reporting strong evidence for a SGWB in this range [1–10]. Hellings-Downs (HD) correlations [11], representing the ‘smoking-gun’ signature of SGWB, have been detected with $2 - 4\sigma$ of statistical significance, depending on the dataset. Upcoming data from PTAs, in particular the joint analysis from IPTA Data Release 3, are expected to further increase the significance of this detection and measure the SGWB amplitude and spectrum more precisely [9]. The observed signal may arise from mergers of supermassive black hole binaries (SMBHB) [12, 13] or from early-universe sources [14] (or a combination of both) and the increasing precision offered by future data may help in identifying the origin of the SGWB. In the longer term, the Square Kilometre Array (SKA) [15, 16], with its unparalleled timing precision and larger number of observed pulsars, will provide definitive measurements of the SGWB properties.

¹nmjc1209.at@gmail.com

²ameek.malhotra.at.swansea.ac.uk

³g.tasinato2208.at@gmail.com

⁴e.i.zavalacarrasco.at.swansea.ac.uk

It is worthwhile to also explore alternative probes that could complement the PTA observations in the nHz regime. One such promising probe is astrometry – using the precise measurements of the positions of a very large number of distant sources to measure the effects of gravitational waves [17–35]. GW present between the Earth and the source induce deflections in the observed positions of these sources (hereafter we lump all such sources under the umbrella term ‘stars’). Much like the pulsar timing residuals, which are correlated across different pulsars as a function of their angular separation, the astrometric deflections for different stars are also correlated, albeit with a slightly different form of the correlation as compared to the PTA HD correlation.

The success of the Gaia mission [36, 37], which observes billions of stars with a precision measurement of their position of the order of the milli-arcsecond (mas), has spurred a renewed interest in astrometric detection of SGWB. Previously, data from Very-long baseline interferometry (VLBI) [38] and more recently Gaia, have already been used to set upper limits on the SGWB in the frequency range 10^{-18} Hz $\lesssim f \lesssim 10^{-9}$ Hz [22, 39–43]. The full Gaia data release 5 (DR5) with the individual time-series measurements will further extend this frequency range to $f \lesssim 4 \times 10^{-7}$ Hz (each star is observed roughly 14 times a year [36]). The upcoming Roman survey [44] – due to its much higher observing cadence – may even be able to push towards higher frequencies ($f \lesssim 10^{-4}$ Hz), opening up an additional observational window for GW [45–47]. Although current astrometric upper limits on the SGWB lie around the $\Omega_{\text{GW}} \lesssim 10^{-2}$ level, the proposed mission Theia [48, 49], with its μas astrometric precision would represent a significant upgrade in terms of sensitivity to SGWB [32, 42, 50], even being competitive with PTA sensitivity.

Motivated by these considerations, in this work we investigate how data from astrometric surveys may be used to complement existing PTA experiments, and potentially improve upon current SGWB measurements obtained from PTA data alone. We do this by means of a Fisher matrix analysis and calculate the improvement in constraints that can be achieved by cross-correlating timing residuals of PTAs with the angular deflections of astrometry, focusing on the parameters corresponding to the SGWB monopole amplitude, spectral tilt (for a power-law spectrum) and a possible dipole anisotropy magnitude. Along the way, we derive for the first time analytic covariant expressions for the response to dipole anisotropy in the SGWB, for astrometry as well as its cross-correlation with PTAs. The anisotropy of the nHz SGWB is a key observable that may be used to discriminate between astrophysical and cosmological origins of the SGWB given their differing predictions, with the magnitude of intrinsic cosmological SGWB anisotropies (see e.g. [51–59]) expected to be much smaller than their astrophysical counterpart [60–68]. Cosmological anisotropies of large magnitude include *kinematic anisotropies* due to our motion with respect to the primordial source of SGWB [58, 69–74]. For primordial sources of SGWB, we can expect a dipolar anisotropy with an amplitude one thousand smaller than the isotropic part of the background, as found in cosmic microwave background measurements [75–78]. Given that kinematic anisotropies of the SGWB are well motivated, we mainly consider a kinematic dipole as specific target for our analysis, although it can be easily extended to discuss other anisotropies as well. Additional works discussing detection prospects of the anisotropies of the SGWB in different contexts are [60, 61, 79–85] with PTA specific analyses in [66, 86–91]. See e.g. [92] for a

review.

This paper is organised as follows: in section 2 we review the theory of SGWB detection with astrometry and corresponding monopole response and overlap reduction functions. We then derive an analytic expression for the astrometric response to the kinematic dipole anisotropy and its auto-correlation. We also discuss the astrometry-redshift correlation for the SGWB monopole and derive an analytic expression for this cross-correlation in the presence of a dipole anisotropy. In section 3, we use these results to forecast the astrometric sensitivity to the SGWB monopole and dipole and also estimate the improvement in constraints that can be obtained by cross-correlating astrometry and PTA data, over PTA data alone. Finally, in section 4, we present our conclusions. Two technical appendixes complement our discussion.

2 Overlap functions for astrometry and pulsar timing arrays

In this section we obtain expressions for astrometric overlap reduction functions (ORF) and their cross-correlations with pulsar timing arrays. We include the possible presence of a dipolar SGWB anisotropy, which can be instrumental for distinguishing cosmological from astrophysical backgrounds. We investigate the crucial role of the position of the monitored objects for determining the sensitivity of the system to the SGWB properties. Our covariant, analytical formulas are convenient and simple to use for Fisher forecast analysis.

Astrometry aims to measure the position and motion of stars on the celestial sphere, while PTA are sensitive to the time of arrival of radio signals from distant pulsar sources. GW passing between the position of stars, pulsars, and the Earth modify photon geodesics, leading to effects which are measurable with both methods. The presence of a stochastic GW background (SGWB) induces correlations among measurements of GW signals, as detected by observations of distinct astronomical objects. In most studies the SGWB is assumed isotropic. However, it develops kinematic anisotropies if the frames of GW source and GW detector move with respect to each other [69]. Kinematic anisotropies break the isotropy of the SGWB, making it direction-dependent: they are fully determined by the properties of the isotropic part of the background, as well as the direction of the velocity among frames. For this reason it is desirable to derive analytical, covariant expressions for the ORF, which make transparent how the sensitivity to SGWB properties depend on the position of stars in the sky. We do so in section 2.1 where we focus specifically on astrometry, while in section 2.2 we analyse its possible synergies with PTA observations.

2.1 Astrometry overlap functions

We define GW in terms of spin-2 fluctuations of the flat metric

$$ds^2 = -dt^2 + [\delta_{ij} + h_{ij}(t, \vec{x})] dx^i dx^j. \quad (2.1)$$

The transverse-traceless spin-2 tensors $h_{ij}(t, \vec{x})$ can be decomposed in Fourier modes as

$$h_{ij}(t, \vec{x}) = \sum_{\lambda} \int_{-\infty}^{+\infty} df \int d^2 \mathbf{p} e^{-2\pi i f \mathbf{p} \cdot \vec{x}} e^{2\pi i f t} \mathbf{e}_{ij}^{\lambda}(\mathbf{p}) h_{\lambda}(f, \mathbf{p}), \quad (2.2)$$

where f is the GW frequency, and \mathbf{p} the unit vector indicating its direction. $\mathbf{e}_{ij}^\lambda(\mathbf{p})$ are real polarization tensors in the basis $\lambda = (+, \times)$. We impose $h_\lambda(-f, \mathbf{p}) = h_\lambda^*(f, \mathbf{p})$. A GW passing between a star and the Earth causes a distortion δn^i on the star direction, \mathbf{n} , at time t , given by the formula (see e.g. [25])

$$\delta n_i(t, \mathbf{n}) = \mathcal{R}_{ikl}(\mathbf{n}, \mathbf{p}) h_{kl}(t, 0) \quad (2.3)$$

where as customary we focus on the so-called ‘Earth-term’ contribution only (see e.g. [25, 93]). We introduce

$$\mathcal{R}_{ikl}(\mathbf{n}, \mathbf{p}) = \frac{n_k}{2} \left[\frac{(n_i + p_i)n_l}{1 + \mathbf{n} \cdot \mathbf{p}} - \delta_{il} \right] \quad (2.4)$$

where recall that the unit vectors \mathbf{n} and \mathbf{p} indicate the direction of the star and of GW propagation, respectively. The three-index quantity \mathcal{R}_{ikl} is orthogonal to the unit vector n_i when contracted with its first index.

In order to characterize a GW signal, we focus on correlation functions of the distortions of star positions. The two-point function of the GW Fourier mode is expressed as

$$\langle h_{\lambda_1}(f_1, \mathbf{p}_1) h_{\lambda_2}^*(f_2, \mathbf{p}_2) \rangle = \frac{3H_0^2}{4\pi^2} \frac{\Omega_{\text{GW}}(f_1, \mathbf{p}_1)}{f_1^3} \delta(f_1 - f_2) \frac{\delta^{(2)}(\mathbf{p}_1 - \mathbf{p}_2)}{4\pi} \quad (2.5)$$

where $\Omega_{\text{GW}}(f, \mathbf{p})$ is the quantity customarily used for characterizing the GW energy density per log frequency interval (see e.g. [94]). The spectral energy density parameter Ω_{GW} is related to the GW intensity, I , through the relation

$$\Omega_{\text{GW}}(f, \mathbf{p}) = \frac{4\pi^2 f^3}{3H_0^2} I(f, \mathbf{p}). \quad (2.6)$$

A SGWB can be characterized by anisotropies, which render $\Omega_{\text{GW}}(f, \mathbf{p})$ explicitly dependent on the GW direction \mathbf{p} . We include here SGWB *kinematic anisotropies* [69], induced by the motion of the observer with respect to the GW background source. They can be a key observable for distinguishing astrophysical from cosmological backgrounds [58, 69]. Denoting with $\beta = |\mathbf{v}|/c$ the size of the relative velocity among frames with respect to the speed of light, and \mathbf{v} the velocity unit vector, we have [69]

$$\Omega_{\text{GW}}(f, \mathbf{p}) = \bar{\Omega}_{\text{GW}}(f) + \beta(4 - n_\Omega) \mathbf{p} \cdot \mathbf{v} \bar{\Omega}_{\text{GW}}(f), \quad (2.7)$$

where $\bar{\Omega}_{\text{GW}}(f) = (4\pi)^{-1} \int d^2\mathbf{p} \Omega_{\text{GW}}(f, \mathbf{p})$ is the angular averaged GW energy density. The result depends also on the energy density spectral tilt $n_\Omega \equiv d \ln \Omega_{\text{GW}} / d \ln f$. The simple form of the SGWB anisotropy of equation (2.7) is all what we need to carry on our calculations. We include only the kinematic dipole contribution proportional to β , working under the hypothesis of small relative velocity among frames – supported by observations of the cosmic microwave background (CMB) dipolar anisotropy of the CMB temperature [75–78]. It is important to emphasize that kinematic effects are associated with deterministic – and not statistical – anisotropies. Hence, formula (2.7) fully characterizes the kinematic dipolar anisotropy, with no need of ensemble averaging. An implication is that our analysis of overlap functions can be conveniently carried on in a fully covariant way.

An alternative method would be to work in the spherical harmonic basis for the timing residuals and angular deflections, e.g. see in [29, 31, 95–97]. For a full-sky survey with a uniform distribution of stars, spherical harmonics provide a convenient diagonal basis for analysing the effects of the SGWB due to the orthogonality of the spherical harmonics. However, in general the dataset used may not have a uniform distribution of sources or be full-sky e.g. see [42]. To keep our analysis completely general and applicable to arbitrary distributions of stars, we do not resort to the spherical harmonic decomposition.

We proceed considering two-point correlators of star deflections as induced by GW passing between stars and the Earth. Denoting with \mathbf{n} and \mathbf{q} the unperturbed directions of the two stars respectively, we use eqs (2.3), (2.5) and (2.7) to find

$$\begin{aligned} \langle \delta n^i(\mathbf{n}, t) \delta n^j(\mathbf{q}, t') \rangle &= \frac{3H_0^2}{32\pi^3} \int df \frac{\bar{\Omega}_{\text{GW}}(f)}{f^3} \cos[2\pi f(t-t')] \left[H_{ij}^{(0)}(\mathbf{n}, \mathbf{q}) + \beta(4 - n_\Omega) H_{ij}^{(1)}(\mathbf{n}, \mathbf{q}, \mathbf{v}) \right], \\ &= p_{(0)} H_{ij}^{(0)}(\mathbf{n}, \mathbf{q}) + p_{(1)} H_{ij}^{(1)}(\mathbf{n}, \mathbf{q}, \mathbf{v}). \end{aligned} \quad (2.8)$$

The quantities $p_{(0,1)}$ depend on integrals along the frequency of the SGWB amplitude and its spectral tilt n_Ω . The tensors $H_{ij}^{(0)}$ and $H_{ij}^{(1)}$ are independent of frequency. They are formally expressed in terms of the following angular integrals

$$H_{ij}^{(0)}(\mathbf{n}, \mathbf{q}) = \int d^2\Omega_{\mathbf{p}} \mathcal{R}_{ikl}(\mathbf{n}, \mathbf{p}) \mathcal{R}_{jrs}(\mathbf{q}, \mathbf{p}) P_{klrs}, \quad (2.9)$$

$$H_{ij}^{(1)}(\mathbf{n}, \mathbf{q}, \mathbf{v}) = \int d^2\Omega_{\mathbf{p}} (\mathbf{p} \cdot \mathbf{v}) \mathcal{R}_{ikl}(\mathbf{n}, \mathbf{p}) \mathcal{R}_{jrs}(\mathbf{q}, \mathbf{p}) P_{klrs}. \quad (2.10)$$

The tensors $H_{ij}^{(0,1)}$ are the analog of the PTA ORF relative to the monopolar and dipolar kinematic components of the SGWB. To compute these quantities, we introduce the projection tensor

$$P_{ijkl} = \delta_{ik}\delta_{jl} + \delta_{il}\delta_{jk} - \delta_{ij}\delta_{kl} + p_i p_j p_k p_l - \delta_{ik} p_j p_l - \delta_{jl} p_i p_k - \delta_{il} p_j p_k - \delta_{jk} p_i p_l + \delta_{ij} p_k p_l + \delta_{kl} p_i p_j \quad (2.11)$$

associated with combinations of polarization tensors $e_{ij}^{(\lambda)}$. The tensors $H_{ij}^{(0,1)}(\mathbf{n}, \mathbf{q})$ are orthogonal to \mathbf{n} in their first index, and to \mathbf{q} in their second index.

The integrals (2.9), (2.10), can be performed with a standard methods of contour integration used in the context of PTA physics, see e.g. [98]. For the case of the monopole, the ORF is associated with the integral in eq (2.9). We consider the combination

$$y = \frac{1 - \mathbf{n} \cdot \mathbf{q}}{2} = \frac{1 - \cos \zeta}{2}. \quad (2.12)$$

controlling the angular separation between a pair of stars on the celestial sphere: this quantity lies in the interval $0 \leq y \leq 1$. The astrometry ORF relative to the monopolar, isotropic component of the SGWB is

$$\begin{aligned} H_{ij}^{(0)}(\mathbf{n}, \mathbf{q}) &= \frac{\pi}{3(1-y)^2} (1 - 8y + 7y^2 - 6y^2 \ln y) \times \\ &[(2 - 2y)\delta_{ij} - n_i n_j - q_i q_j - q_i n_j + (1 - 2y)q_j n_i], \end{aligned} \quad (2.13)$$

a result equivalent to what was found in [25], although expressed slightly more compactly. As mentioned above, we obtained this expression by evaluating the integral (2.9) using contour integration. The expression (2.13) is the astrometry equivalent of the Hellings-Downs function, the PTA ORF for the SGWB monopole. In the case of astrometry, the value of (2.13) depends on the angular separation $\mathbf{n} \cdot \mathbf{q}$ between stars, as well as more specifically on the star directions n_i and q_j .

The tensor defined by the integral (2.10) corresponds instead to the astrometry response function for dipolar kinematic anisotropies. It can be computed in terms of appropriate spherical harmonics [31] – but we provide here a covariant, succinct expression for it. We introduce, as in [25], a basis of vectors:

$$\mathbf{A} = \mathbf{n} \times \mathbf{q} \quad , \quad \mathbf{B} = \mathbf{n} \times \mathbf{A} \quad , \quad \mathbf{C} = -\mathbf{q} \times \mathbf{A} . \quad (2.14)$$

Computing the integral of eq (2.10) by means of contour integrations, we find

$$H_{ij}^{(1)} = a_1 (A_i C_j + B_i A_j) + a_2 (B_i C_j - A_i A_j) , \quad (2.15)$$

with $a_{1,2}$ scalar coefficients depending on the angles among the vectors involved. Recalling the definition (2.12), and denoting

$$(Av) = \mathbf{v} \cdot (\mathbf{n} \times \mathbf{q}) \quad , \quad (nv) = \mathbf{n} \cdot \mathbf{v} , \quad (2.16)$$

we express the coefficients $a_{1,2}$ as

$$a_1 = \frac{\pi(Av) \left(1 - 4y - \frac{3y^2 \ln(y)}{1-y}\right)}{6y(1-y)^2} , \quad (2.17)$$

$$a_2 = \frac{\pi[(y-1)(2y+1) - 3y \ln(y)] \left[2(nv)(1-y) + \sqrt{4(1-nv)^2(1-y)y - (Av)^2}\right]}{6(1-y)^3} . \quad (2.18)$$

Our analytical, covariant expressions (2.13) and (2.15) for the ORF demonstrate that the astrometry sensitivity to the SGWB depend not only on the angle among stars, ζ , but also on their position in the sky, and on the velocity vector \mathbf{v} among frames.

The compact expressions (2.13) and (2.15) are particularly suitable to visualise patterns of sensitivity on the celestial sphere, and to further explore geometrical features of physically relevant quantities in the context we are examining. We plot in Figure 1 the combinations

$\text{Tr}[\mathbf{H}_0 \mathbf{H}_0]$ and $\text{Tr}[\mathbf{H}_1 \mathbf{H}_1]$, representative of the sensitivity of astrometry observations to the monopole (through the function \mathbf{H}_0) and the dipole (through the function \mathbf{H}_1).⁵ (Further theoretical motivations for considering such combinations are developed in section 3.) We introduce here the shorthand notation $\mathbf{H}_{0,1}$ to more compactly express the matrices involved with components $H_{ij}^{(0,1)}$. The quantity $\text{Tr}[\mathbf{H}_0 \mathbf{H}_0]$ does not depend on the velocity \mathbf{v} among frames, and

⁵A dipolar anisotropy induces also a correlation between the electric E and magnetic B components of the angular deflection correlation functions. We explore this topic in Appendix A.

its magnitude depends only on the angle ζ between the stars, as defined in eq (2.12). (See also Appendix B for analytical expressions of the combinations we plot.) In the upper left panel of Figure 1 we analyse the quantity $\text{Tr}[\mathbf{H}_0\mathbf{H}_0]$ in the case where one of the star directions \mathbf{n} points to the centre of the sky map; the function reaches its local maxima at $\zeta = 0^\circ$ and $\zeta \approx 105.6^\circ$, and has two roots at $\zeta = 180^\circ$ and $\zeta \approx 57.10^\circ$. Such features are also represented on the left panel of Figure 2. Next, the quantity $H_{ij}^{(1)}$ controls the sensitivity to the kinematic dipole, and depends not only on the angle between the stars, but also on the angle between the velocity \mathbf{v} and the stars' directions. See eq (2.15). In the lower panels of Figure 1 we present two maps to represent the properties of this function. Complex patterns for the ORF sensitivity to GW arise, depending on the direction of star positions in the sky. Nevertheless, we can consider a simple scenario where \mathbf{n} is parallel to \mathbf{v} . This assumption simplifies the expression for $\text{Tr}[\mathbf{H}_1\mathbf{H}_1]$, and allows us to appreciate the system sensitivity to SGWB properties only in terms of the angle separation ζ among the stars. In the upper right panel of Figure 1 the red band represents the regions of higher sensitivity. The maximum of the function is reached at $\zeta \approx 119.45^\circ$, while the blue regions represent the lowest values of the function, including its three roots at $\zeta = 0, \pi$ and $\zeta \approx 73.14^\circ$. The resulting behaviour is also represented in the right panel of Figure 2.

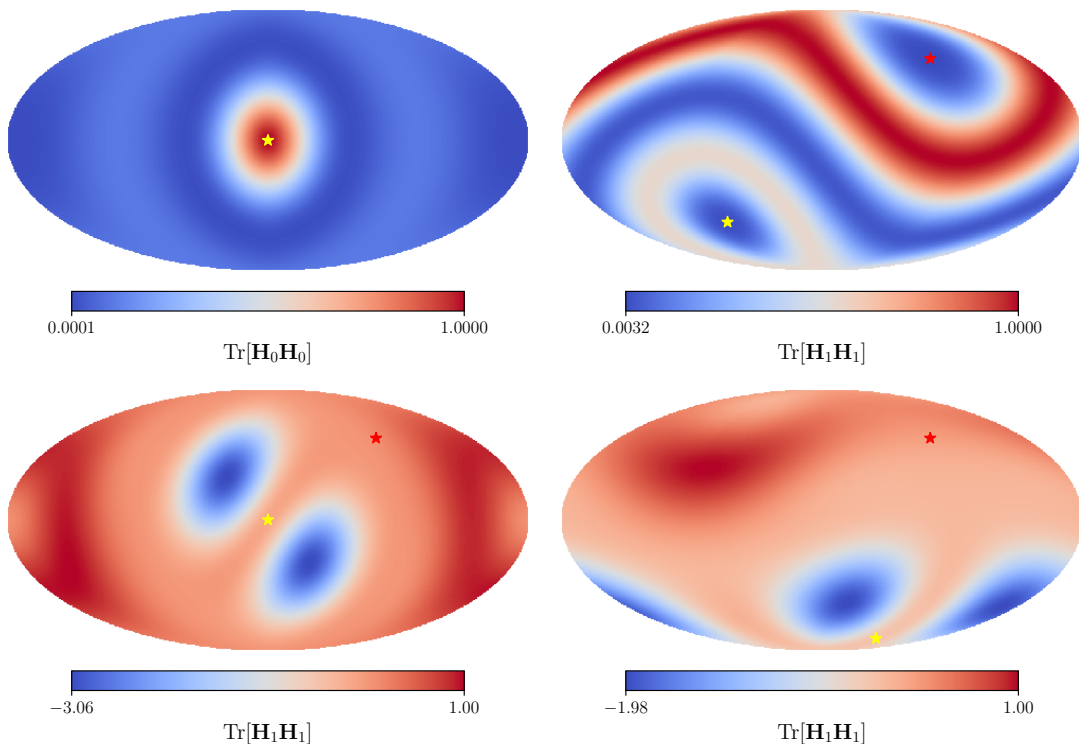


Figure 1: The quantities $\text{Tr}[\mathbf{H}_0\mathbf{H}_0]$ and $\text{Tr}[\mathbf{H}_1\mathbf{H}_1]$, associated with response to a SGWB depending on stars positions. (See the main text for our notation.) Motivated by CMB, we choose the kinematic dipole direction \mathbf{v} (red star) at $(l, b) = (264^\circ, 48^\circ)$ in galactic coordinates. Each panel shows a different choice of \mathbf{n} , while the stars \mathbf{q} take the position of each pixel of the map. **Upper left panel:** \mathbf{n} pointing towards $(l, b) = (0, 0)$. **Upper right panel:** \mathbf{n} pointing towards $-\mathbf{v}$. **Lower left panel:** \mathbf{n} at $(l, b) = (0, 0)$. **Lower right panel:** \mathbf{n} pointing towards the direction $(l, b) = (270.21^\circ, -75.45^\circ)$.

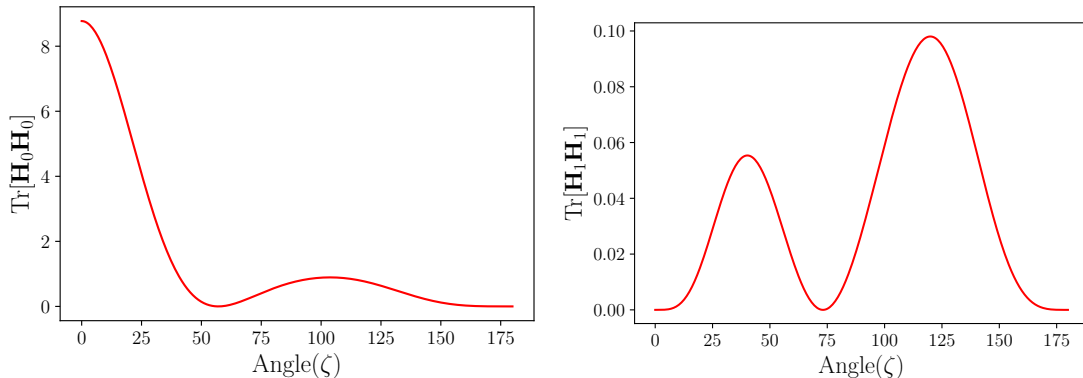


Figure 2: Overlap functions response in terms of the angle between the stars. **Left:** Angular dependence for $\text{Tr}[\mathbf{H}_0 \mathbf{H}_0]$. **Right:** $\text{Tr}[\mathbf{H}_1 \mathbf{H}_1]$ when choosing $\mathbf{n} = -\mathbf{v}$.

2.2 Cross-correlated overlap functions of astrometry and PTA

In the future, precise astronomical observations will improve astrometry measurements, making them more sensitive to GW. The synergy of astrometry and PTA will be instrumental for increasing the sensitivity to the properties of the SGWB. It is therefore important to analytically compute the overlap functions associated with cross correlations between astrometry deflections and pulsar timings, also including effects of SGWB anisotropies. These topics have been explored in [28,29,31]. We present here covariant expressions for the overlap functions of cross correlations, which are convenient for numerical analysis and for the forecasts we carry on in section 3.

We consider two-point correlation functions of deflections of star positions, and of pulsar time delays $z(t) = \Delta T(t)/T(t)$, where $T(t)$ is the total time the radio signal needs for travelling from the pulsar source to the detector. We denote with \mathbf{x} the unit vector pointing from the Earth towards the specific pulsar being monitored. The time delay induced by a GW propagating along the direction \mathbf{p} results (see e.g. [93])

$$z(t) = \frac{1}{2} \frac{x^i x^j}{1 + \mathbf{x} \cdot \mathbf{p}} h_{ij}(t, 0), \quad (2.19)$$

where we include the Earth term only [93]. This piece of information, together with the results of section 2.1, allow us to compute the correlation functions between star deflection $\delta n^i(\mathbf{n}, t)$ and $z(t)$, induced by the presence of a SGWB. It reads

$$\langle \delta n_i(\mathbf{n}, t) z(t) \rangle = \frac{3 H_0^2}{64 \pi^3} \int df \frac{\bar{\Omega}_{\text{GW}}(f)}{f^3} \left[K_i^{(0)}(\mathbf{n}, \mathbf{x}) + \beta (4 - n_\Omega) K_i^{(1)}(\mathbf{n}, \mathbf{x}, \mathbf{v}) \right]. \quad (2.20)$$

In analogy with the formulas developed in section 2.1, the quantities $K_i^{(0)}$ and $K_i^{(1)}$ denote respectively the cross-correlated overlap reduction functions relative to the SGWB monopole, and kinematic dipole. Using the same notation of previous section, they are expressed in terms of the angular integrals

$$K_i^{(0)}(\mathbf{n}, \mathbf{x}) = \int d^2 \Omega_{\mathbf{p}} \mathcal{R}_{ikl}(\mathbf{n}, \mathbf{p}) P_{klrs} \frac{x^r x^s}{1 + \mathbf{x} \cdot \mathbf{p}} \quad (2.21)$$

$$K_i^{(1)}(\mathbf{n}, \mathbf{x}, \mathbf{v}) = \int d^2\Omega_{\mathbf{p}} (\mathbf{p} \cdot \mathbf{v}) \mathcal{R}_{ikl}(\mathbf{n}, \mathbf{p}) P_{klrs} \frac{x^r x^s}{1 + \mathbf{x} \cdot \mathbf{p}} \quad (2.22)$$

These integrals can be computed straightforwardly through contour integration in the complex plane. It is convenient to express the results in terms of the quantity (not to be confused with the analogous quantity (2.12) of Section 2.1)

$$y = \frac{1 - \mathbf{n} \cdot \mathbf{x}}{2} \quad (2.23)$$

related to the angle between the direction of the monitored star and pulsar. The ORF of the cross-correlation monopole reads

$$K_i^{(0)}(\mathbf{n}, \mathbf{x}) = \frac{16\pi}{3} \frac{(1 - 2y) n_i - x_i}{4y(1 - y)} (2y - 2y^2 + 3y^2 \ln(y)) \quad (2.24)$$

a formula equivalent to the one found in [28], although expressed in another form.

The overlap function for the kinematic dipole is more easily expressed in terms of two vectors $\mathbf{A}_{1,2}$ orthogonal to the star direction \mathbf{n} :

$$\mathbf{A}_1 = \mathbf{n} \times \mathbf{x}, \quad (2.25)$$

$$\mathbf{A}_2 = \mathbf{n} \times \mathbf{v}. \quad (2.26)$$

Notice the identity $\mathbf{A}_1 \cdot \mathbf{A}_2 = \mathbf{x} \cdot \mathbf{v} - (\mathbf{n} \cdot \mathbf{v})(\mathbf{n} \cdot \mathbf{x})$. We parameterize the dipolar overlap function as

$$K_i^{(1)}(\mathbf{n}, \mathbf{x}) = b_1 A_{1i} + b_2 A_{2i}. \quad (2.27)$$

We denote $\mathbf{A}_1 \cdot \mathbf{v} = (A_1 v)$, etc. The two coefficients $b_{1,2}$ can be computed by contour integration, and result ⁶

$$b_1 = \frac{\pi \left((A_1 v)^2 (1 - 12y) + (A_1 A_2) \left((A_1 A_2) + 12(A_1 A_2) y^2 + 4(nv) y (1 + y(5 - 6y)) \right) \right)}{6(A_1 v)(1 - y)y} + \frac{2\pi \left((A_1 A_2)^2 - (A_1 v)^2 + 2(A_1 A_2)(nv)(1 - y) \right) y \ln(y)}{(A_1 v)(1 - y)^2}, \quad (2.29)$$

$$b_2 = -\frac{2\pi \left((A_1 A_2) + 12(A_1 A_2) y^2 + 4(nv) y (1 + y(5 - 6y)) \right)}{3(A_1 v)} - \frac{8\pi \left((A_1 A_2) + 2(nv)(1 - y) \right) y^2 \ln(y)}{(A_1 v)(1 - y)}. \quad (2.30)$$

Analogously to our discussion towards the end of section 2.1, we can visualise the ORF for astrometry working in synergy with PTA experiments. They are controlled by the combinations $\mathbf{K}_0 \mathbf{K}_0^T$ and $\mathbf{K}_1 \mathbf{K}_1^T$. We denote more compactly the vectors $K_i^{(0,1)} \equiv \mathbf{K}_{0,1}$.

⁶The expression (2.27) is valid for all values of angles among the vectors involved, apart from when $\mathbf{n} \cdot \mathbf{v} = 0$. Then the vector \mathbf{A}_2 vanishes, as well as the product $\mathbf{A}_1 \cdot \mathbf{v}$. The limit $\mathbf{n} \cdot \mathbf{v} \rightarrow 0$ is hence delicate. For this specific case of velocity vector \mathbf{v} parallel to the star direction \mathbf{n} , the expression for the dipole response function reduces to

$$K_i^{(1)}(\mathbf{n}, \mathbf{x}) = \frac{2\pi(n_i(1 - 2y) - x_i)}{3(1 - y)} ((y - 1)(6y + 1) - 6y \ln(y)). \quad (2.28)$$

We call ζ_{sp} the angle between star and pulsar directions, $\cos \zeta_{sp} = \mathbf{n} \cdot \mathbf{x}$. We represent a simple example in the upper left panel of Figure 3 with \mathbf{n} pointing towards $(l, b) = (0, 0)$; the roots of the function $\mathbf{K}_0 \mathbf{K}_0^T$ are at $\zeta_{sp} = 0, \pi$ and $\zeta_{sp} \approx 86.14^\circ$, while its local maxima are located at $\zeta_{sp} \approx 37.13^\circ$ and $\zeta_{sp} \approx 132.195^\circ$, and are represented in the left panel of Figure 4. The lower panel of Figure 3 shows two scenarios for the general expression for the function $\mathbf{K}_1 \mathbf{K}_1^T$ (see also Appendix B), which depends on the angle between star and pulsar and the angle between the velocity and pulsars given by $vx = \mathbf{v} \cdot \mathbf{x}$; on the left we choose \mathbf{n} at $(l, b) = (0, 0)$, and on the right, \mathbf{n} is at position $(l, b) = (270.21^\circ, -75.45^\circ)$ (a direction chosen randomly). The sensitivity patterns are complex. However, in the specific case of the star direction \mathbf{n} pointing towards the direction $-\mathbf{v}$ we obtain a simple formula, depending only on the angle between star and pulsar. This last case is shown on the right upper panel of Figure 3, where the bluest, less sensitive regions showing the positions of objects at relative angle $\zeta_{sp} = 0, \pi$ and $39.82^\circ, 101.37^\circ$, corresponding to minimal sensitivity to dipole. The red region shows the positions of the pulsars where the function $\mathbf{K}_1 \mathbf{K}_1^T$ reaches its maximum at $\zeta_{sp} \approx 142.29^\circ$. There are also local maxima at $\zeta_{sp} \approx 17.97^\circ, 71.88^\circ$, which are more apparent on the right panel of Figure 4. Notice that the quantities $\mathbf{K}_{0,1}$ corresponding to the synergetic ORF vanish in the coincident limit of the star aligned with the pulsar direction. One may understand this as follows – the star deflection always lies in the plane perpendicular to the line of sight. On the contrary, the pulsar timing residual arises from the change in length along the line of sight. Thus for pulsar and star in same direction the two effects are perpendicular to each other.

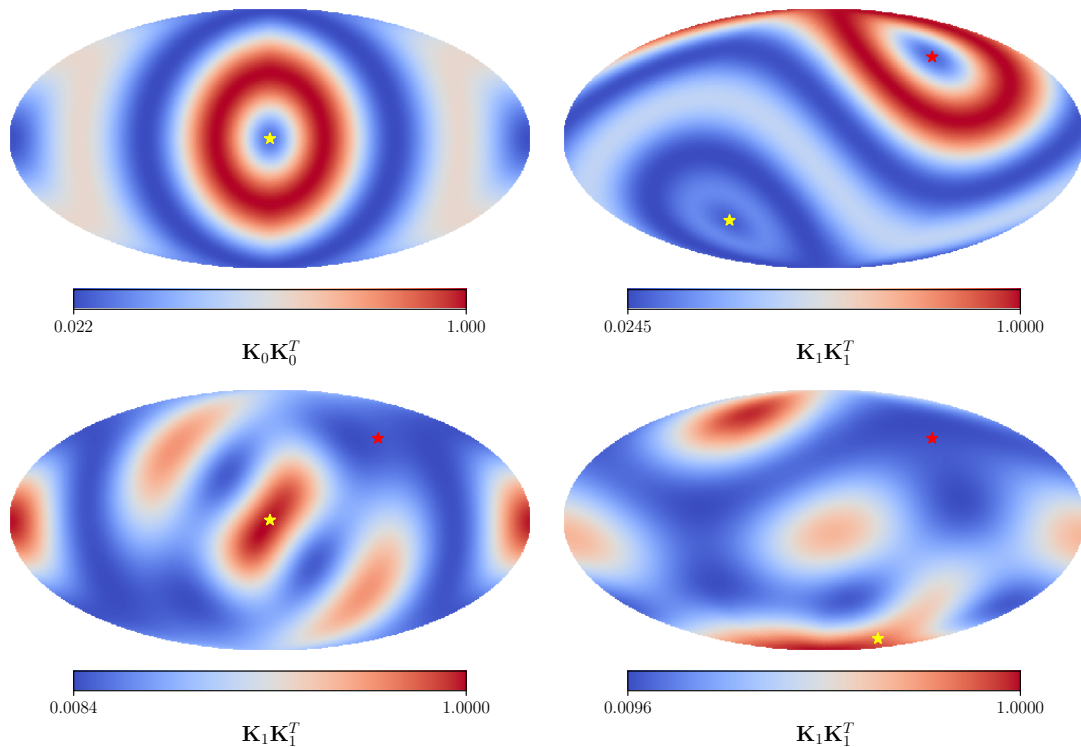


Figure 3: The quantities $\mathbf{K}_0 \mathbf{K}_0^T$, and $\mathbf{K}_1 \mathbf{K}_1^T$ response to stars and pulsars positions. The dipole direction \mathbf{v} (red star) is chosen in the direction $(l, b) = (264^\circ, 48^\circ)$ in galactic coordinates. Each panel shows a different choice of \mathbf{n} , while the pulsars positions \mathbf{x} scan over each pixel of the map. **Upper left panel:** \mathbf{n} towards $(l, b) = (0, 0)$. **Upper right panel:** \mathbf{n} towards $-\mathbf{v}$. **Lower left panel:** \mathbf{n} at $(l, b) = (0, 0)$. **Lower right panel:** \mathbf{n} towards $(l, b) = (270.21^\circ, -75.45^\circ)$.

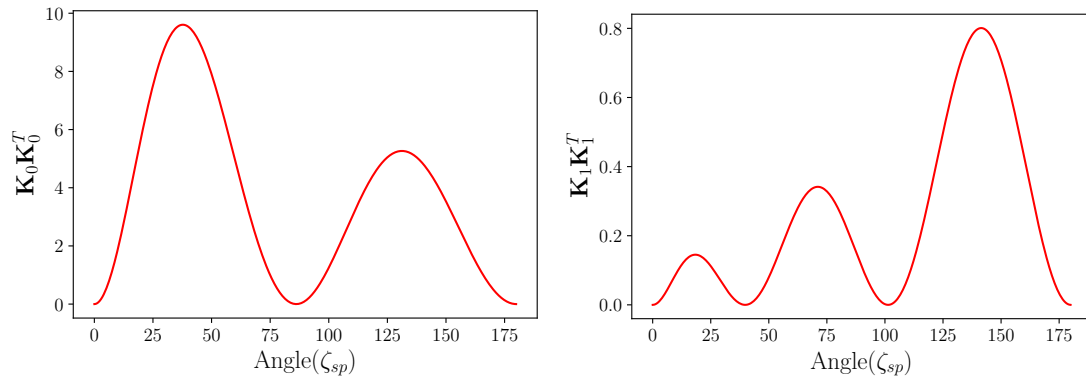


Figure 4: Overlap functions response in terms of the angle between the stars and pulsars. **Left:** Angular dependence for $\mathbf{K}_0 \mathbf{K}_0^T$. **Right:** The quantities $\mathbf{K}_1 \mathbf{K}_1^T$ when choosing $\mathbf{n} = -\mathbf{v}$.

3 Optimal estimators, and Fisher forecasts

Armed with the covariant, analytical expressions we derived for the ORF of astrometry and PTA systems – including the effects of kinematic anisotropies – in this section we investigate the prospects of future experiments to characterize the SGWB. We are interested in measuring

the SGWB amplitude, its spectral tilt, as well as the magnitude of a possible dipolar anisotropy characterizing the SGWB. We quantify how the results depend on the number of astronomical objects we measure, as well as on the precision of their measurement.

In section 3.1 we determine the general optimal estimators to detect the SGWB properties, and show how they depend on the star through the ORF determined in Section 2. Based on such general estimators, we build a Gaussian likelihood and derive concise expressions for the Fisher matrix, whose structure depend in a transparent way on the geometrical properties of the systems we consider. In appropriate limits and special cases, the Fisher matrix obeys interesting scaling relations which make our analysis particularly simple. In general though, numerical work is needed to evaluate at what extent the synergy between astrometry and PTA improve the sensitivity to SGWB properties. We carry out such analysis in sections 3.2, 3.2.3, making use of the weak signal approximation for astrometry to simplify the numerical calculations for a large number of stars.

3.1 Building the optimal estimator: the case of astrometry

We start by discussing the case of astrometry only. We expand the deflection correlation of eq (2.8) in a basis with coefficients p_n ,

$$\langle \delta n_a^i \delta n_b^j \rangle \equiv \mathbf{C} = \sum_{n=1,2} p_n H_{ab,n}^{ij} + N_{ab}^{ij} = \sum_{n=1,2} p_n \mathbf{H}_n + \mathbf{N}. \quad (3.1)$$

The indexes a, b identify the two stars. i, j the three-dimensional vector components, and the index n runs over 1, 2 indicating monopolar and dipolar contributions to the signal. We include the effects of noise controlled by the noise matrix N_{ab}^{ij} . The quantities p_n and $H_{ab,n}$ are controlled by the properties of the SGWB, as well as the astrometry ORF. See equation (2.8) and the discussion that follows for the definitions. At this stage, we do not need to specify whether we work either in time or in frequency domain. Our aim is to determine the quantities $p_{0,1}$, and extract from this information the properties of the SGWB: its monopole amplitude Ω_{GW} as well as the value of the parameter β controlling kinematic anisotropies.

Before proceeding to build the optimal estimators, we notice that the matrix C can not be directly be used as a covariance matrix, since it is singular. This stems from the fact that the three Cartesian deflection components are not independent since observations get projected on to the two-dimensional celestial sphere. Hence, the star deflections can be entirely described in terms of two angles $\delta\theta$ and $\delta\phi$ [28]. Let P be the matrix that converts the deflections from 3D Cartesian to 2D polar coordinates, i.e.

$$\begin{pmatrix} \delta\theta \\ \delta\phi \end{pmatrix} = P \cdot \begin{pmatrix} \delta x \\ \delta y \\ \delta z \end{pmatrix}. \quad (3.2)$$

The matrix P is used to convert the original correlation matrix for the Cartesian deflections to a correlation matrix in terms of angular deflections. For a single star, it is given by [28]

$$P = \begin{bmatrix} 0 & 0 & \frac{1}{\sqrt{1-z^2}} \\ -\frac{y}{x^2+y^2} & \frac{x}{x^2+y^2} & 0 \end{bmatrix}. \quad (3.3)$$

For the full system of N stars, the projection matrix R can be written in block diagonal form [28]

$$R = \begin{bmatrix} P_1 & 0 & \dots & 0 \\ 0 & P_2 & \dots & 0 \\ \vdots & \vdots & \ddots & \vdots \\ 0 & 0 & \dots & P_n \end{bmatrix}. \quad (3.4)$$

This can be used to obtain the angular deflection covariance matrix from the Cartesian one

$$C_{ij}^{\delta\theta} = R \cdot C_{ij}^{\delta\vec{x}} \cdot R^T. \quad (3.5)$$

Keeping this in mind, we now derive general expressions for our estimator of the coefficients p_n formally appearing in the sum (3.1), later specialising to the monopole and dipole case with p_0 and p_1 . The determination of these coefficients allows us to infer the properties of the SGWB.⁷ A quadratic estimator for p_n can be formally expressed as

$$\hat{p}_n = \delta n_a^i E_{ab,n}^{ij} \delta n_b^j - b_n, \quad (3.6)$$

in terms of a matrix $E_{ab,n}$ and a vector b_n . We wish to determine the corresponding values of these quantities which render the estimator unbiased, and minimizes its variance.

Following the procedure developed in [99] (see also [100]), we find

$$\langle \hat{p}_n \rangle = \sum_{n'} W_{nn'} p_{n'} + \text{Tr}[\mathbf{E}_n \mathbf{N}] - b_n, \quad \text{with} \quad W_{nn'} \equiv \text{Tr}[\mathbf{H}_{n'} \mathbf{E}_n]. \quad (3.7)$$

Thus, the quantity b_n should be chosen as $b_n = \text{Tr}[\mathbf{E}_n \mathbf{N}]$ to ensure that the estimator is unbiased. We now calculate the variance of estimator (3.6), in order to minimise it. We impose $W_{nn} = 1$ as overall normalisation. The variance is given by

$$\text{Cov}(p_n, p_{n'}) = 2\text{Tr}[\mathbf{C} \mathbf{E}_n \mathbf{C} \mathbf{E}_{n'}] \quad (3.8)$$

The matrix \mathbf{E}_n is⁸

$$\mathbf{E}_n = \frac{\mathbf{C}^{-1} \mathbf{H}_n \mathbf{C}^{-1}}{\text{Tr}[\mathbf{C}^{-1} \mathbf{H}_n \mathbf{C}^{-1} \mathbf{H}_n]}. \quad (3.9)$$

Hence the unbiased, optimal estimator for p_n is obtained by inverting the resulting matrix $W_{nn'}$:

$$\tilde{p}_n = \sum_{n'} [W]_{nn'}^{-1} \hat{p}_{n'}, \quad (3.10)$$

while the corresponding inverse covariance matrix is given by

$$\text{Cov}^{-1}(\tilde{p}_n, \tilde{p}_{n'}) = \frac{1}{2} \text{Tr}[\mathbf{C}^{-1} \mathbf{H}_n \mathbf{C}^{-1} \mathbf{H}_{n'}]. \quad (3.11)$$

⁷In principle, these basis coefficients can also be spherical harmonics coefficients or individual pixels used to discretize the SGWB intensity map. Our analysis represents a special case where we only expand the SGWB intensity up to the dipole term, assuming a known dipole direction.

⁸In the noise dominated limit with the diagonal noise, the solution reduces to $\mathbf{E}_n = \mathbf{H}_n / \text{Tr}[\mathbf{H}_n \mathbf{H}_n]$, and $W_{nn'} = \text{Tr}[\mathbf{H}_n \mathbf{H}_{n'}] / \text{Tr}[\mathbf{H}_n \mathbf{H}_n]$

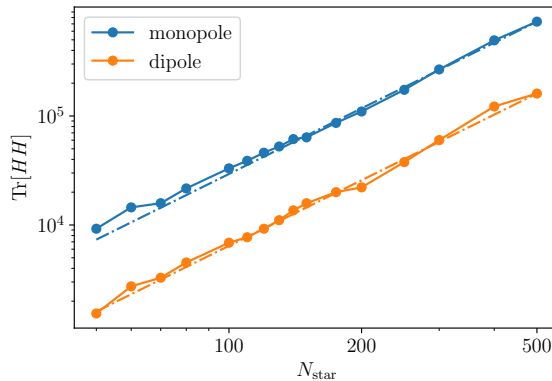


Figure 5: The components of the Fisher matrix (3.13) are evaluated numerically as a function of the number of stars with the stars uniformly distributed across the sky. The dashed lines have slope N_{star}^2 and pass through the numerically evaluated result for $N_{\text{star}} = 500$. This plot numerically confirms eqs (3.14) and (3.15).

In fact, this quantity corresponds to the Fisher matrix for the parameters p_n , assuming they are Gaussian distributed. I.e. we consider a likelihood L of the form

$$-2 \ln L = \delta n_a^i [C^{-1}]_{ab}^{ij} \delta n_b^j + \ln \det C + n \ln 2\pi. \quad (3.12)$$

Specialising to the case where p_0 and p_1 correspond to monopole and dipole as in eq (3.1), in the noise dominated limit with $N_{ab}^{ij} = \sigma^2 \delta_{ab} \delta^{ij}$, we obtain the Fisher matrix \mathcal{F} for the estimators

$$\mathcal{F} = \frac{1}{2\sigma^4} \begin{pmatrix} \text{Tr}[\mathbf{H}_0 \mathbf{H}_0] & \text{Tr}[\mathbf{H}_0 \mathbf{H}_1] \\ \text{Tr}[\mathbf{H}_0 \mathbf{H}_1] & \text{Tr}[\mathbf{H}_1 \mathbf{H}_1] \end{pmatrix}. \quad (3.13)$$

Hence, in the noise-dominated regime, the Fisher matrix depends only on the ORF to the monopole and dipole of the SGWB, discussed in Section 2. The error in determining the individual parameters p_i we are interested in is given by $\Delta p_i = \sqrt{[\mathcal{F}^{-1}]_{ii}}$.

The entries of the Fisher matrix (3.13) simplify under certain hypothesis. For example, we find the following scaling relations which hold in the limit of large $N_{\text{star}} \gg 100$ stars distributed uniformly across the sky (see Figure 5):

$$\mathcal{F}_0 \equiv \text{Tr}[\mathbf{H}_0 \mathbf{H}_0] \simeq 3 \times N_{\text{star}}^2 \quad (3.14)$$

$$\mathcal{F}_1 \equiv \text{Tr}[\mathbf{H}_1 \mathbf{H}_1] \simeq 0.65 \times N_{\text{star}}^2 \quad (3.15)$$

In the same limit, the cross terms depending on $\text{Tr}[\mathbf{H}_0 \mathbf{H}_1]$ vanish in eq (3.13). In practice, to perform Fisher forecasts by means of Eq (3.13) we focus on the frequency domain, performing a frequency binning with $\Delta f = 1/T_{\text{obs}}$, with $T_{\text{obs}} = 15$ years, and summing over the Fisher matrices at each frequency bin. We relate the value of the GW energy density Ω_{GW} to the intensity through equation (2.6). We assume for the latter a power-law ansatz $I(f) \propto f^{3-\gamma}$, and report our results in Fig 6 for different values of spectral slope, also indicating the detection threshold indicated by the IPTA joint analysis [9].

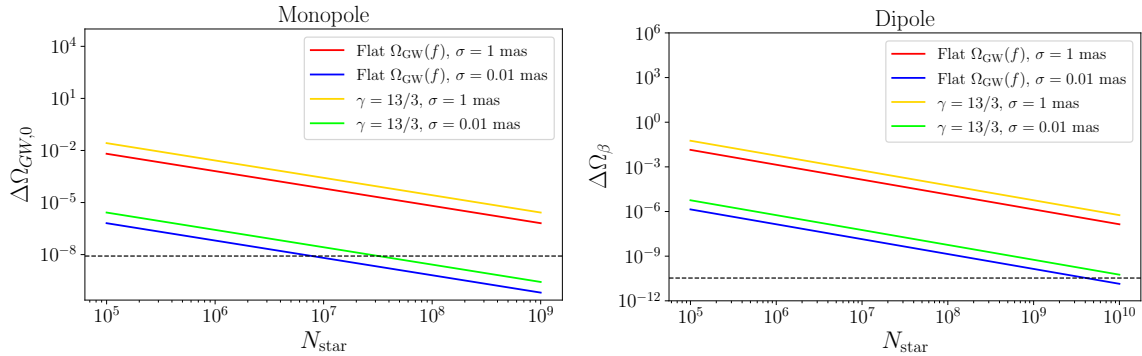


Figure 6: Forecasts for the magnitude of the SGWB energy density and dipolar anisotropy, as measured with astrometry. See the discussion after eq (3.15). **Left:** The error $\Delta\Omega_{\text{GW},0}$ associated with the monopole estimator p_0 . **Right:** $\Delta\Omega_\beta$ associated with the dipole estimator p_1 . We define $\Omega_\beta = \beta(4 - n_\Omega)\Omega_{\text{GW},0}$.

The noise in the frequency domain is given by $\sigma_f^2 = 2\sigma^2 T_{\text{cad}}$. We take different values of σ as shown in Figure 6 and the observational cadence $T_{\text{cad}} = \text{year}/15$, corresponding approximately to the observational cadence of Gaia [36].

Under the assumptions leading to eqs (3.14) and (3.15) we find that astrometric surveys with 0.01 milli-arcsecond (mas) precision which monitor $N > 10^6$ stars may be competitive with PTA experiments, in terms of sensitivity to the SGWB. The detection of the kinematic dipole, whose amplitude is suppressed by a factor β relative to the monopole, will accordingly require about 10^3 times more stars. We should note, though, that for the green line shown in fig. 6, the weak signal approximation likely breaks down, as we go towards a higher and higher number of stars ($N_{\text{star}} \gtrsim 10^6$). The noise level $\sigma = 0.01$ mas roughly corresponds to the expected astrometric accuracy that will be achieved by Gaia DR5 for the brightest objects in the survey.⁹ Thus, the forecast sensitivity with this value of the noise is very unlikely to be achieved in real Gaia DR5 data but may be possible with future missions like Theia [48–50].

3.2 Forecasts: astrometry in synergy with PTA

We now turn our attention to estimators and forecasts for astrometry in synergy with PTA. In this section we consider only the isotropic part of the background, focusing on the amplitude and spectral tilt of the SGWB. The effect of the kinematic dipole is investigated in section 3.2.3.

Let δt_a , $a = 1, 2, \dots, N$, and $\delta \vec{\theta}_b$, $b = 1, 2, \dots, M/2$ be the Fourier transforms of timing residuals and angular deflections of N pulsars and $M/2$ stars respectively.¹⁰ We work under the assumption of a Gaussian distributed SGWB with zero mean. The joint covariance matrix at a

⁹<https://www.cosmos.esa.int/web/gaia/science-performance>

¹⁰The factor of two arises for the stars because they are each characterized by two angular deflections in the sky, while pulsars only by a single time delay.

given frequency can be written in block form as

$$C_{(N+M)\times(N+M)} = \begin{bmatrix} A_{N\times N} & B_{N\times M} \\ B_{M\times N}^T & D_{M\times M} \end{bmatrix}, \quad (3.16)$$

and the joint likelihood as

$$-2 \ln L = (\vec{\delta t}, \vec{\delta \theta}) \cdot C^{-1} \cdot (\vec{\delta t}, \vec{\delta \theta})^T + \ln \det C + \frac{(M+N)}{2} \ln 2\pi. \quad (3.17)$$

As explained previously, we are going to split in frequency bins the total frequency interval we analyse.

The individual sub-matrices A, B, D denote the pulsar-pulsar, pulsar-star and star-star covariance matrices respectively. Notice that they have very different dimensionalities, since we expect to monitor many more stars than pulsars (more on this later). They read

$$A_{pq} = \frac{\gamma_{pq} I_f}{(4\pi f)^2} + \sigma_p^2 \delta_{pq}, \quad (3.18)$$

$$B_{pa} = \frac{K_{p,a} I_f}{4\pi f}, \quad (3.19)$$

$$D_{ab} = H_{ab} I_f + \delta_{ab} \sigma_a^2. \quad (3.20)$$

The tensor γ_{pq} corresponds the standard Hellings-Downs inter-pulsar correlation between pulsar time delays, while $K_{p,a}$ and H_{ab} denote the pulsar-star and star-star correlations studied in section 2. In general, the covariance matrices depend explicitly on the SGWB intensity I_f evaluated at the frequency bin under examination. (We use the same notation as [101, 102].)

The Fisher matrix for the joint forecast is given by the usual formula [103]

$$\mathcal{F}_{\alpha\beta} = \frac{1}{2} \text{Tr}[C^{-1} C_\alpha C^{-1} C_\beta]. \quad (3.21)$$

where C_α denotes the derivative with respect to the parameter α . We wish to investigate how the addition of the astrometric datasets can help to improve upon on the constraints on the SGWB amplitude and spectral tilt, with respect to an analysis based only on PTA data.

We first calculate the inverse of our covariance matrix. When the matrices A and D are both invertible, as is the present case, the inverse is given by [104, 105]

$$C^{-1} = \begin{bmatrix} (A - BD^{-1}B^T)^{-1} & 0 \\ 0 & (D - B^T A^{-1} B)^{-1} \end{bmatrix} \begin{bmatrix} \mathbf{1}_N & -BD^{-1} \\ -B^T A^{-1} & \mathbf{1}_M \end{bmatrix}. \quad (3.22)$$

While the derivative C_α reads

$$C_\alpha = \begin{bmatrix} A_\alpha & B_\alpha \\ B_\alpha^T & D_\alpha \end{bmatrix}. \quad (3.23)$$

3.2.1 Some concrete examples

To demonstrate in concrete how the cross-correlation of astrometric and PTA data can be useful to characterize the SGWB signal – even when the astrometric data alone are not very constraining – we start with a simple example. **Case 1:** We parameterize the SGWB intensity as

$$I(f) = \frac{A_{\text{GW}}^2}{2} \left(\frac{f}{f_{\text{ref}}} \right)^{3-\gamma}, \quad (3.24)$$

with $f_{\text{ref}} = 1/\text{year}$. We choose PTA parameters so as to recover the level of constraints set by the IPTA joint analysis [9] with 15 years of observation time, roughly corresponding to $\log_{10} A_{\text{GW}} = -14.6 \pm 0.16$, $\gamma = 13/3 \pm 0.45$ at 95% C.L. For the astrometric analysis, we take 1000 stars with identical noise level $\sigma_S^2 = 2[\Delta\theta_{\text{rms}}]^2 T_{\text{cad}}$ with $\Delta\theta_{\text{rms}} = 0.001 \text{ mas}$ and $T_{\text{cad}} = \text{year}/24$, i.e. with each star observed twice per month.

Although typical astrometric datasets have a larger number of stars, and at the same time larger noise levels, this example suffices to make our point. Both the pulsar and the star configuration is supposed to be distributed uniformly across the sky.

The signal strength, frequency binning (with bin width $\Delta f = 1/T_{\text{obs}}$) and noise levels are plotted in the left panel of fig. 7. In the right panel of the same figure we plot the Fisher forecast for the parameters $\log A_{\text{GW}}$ and γ within this setup. We learn that the joint PTA+Astrometric dataset does provide an improvement over the PTA-only constraints, even when the astrometric data alone is not too informative. Nearly identical results are obtained on changing the number of stars while at the same time rescaling the noise using

$$\Delta\theta_{\text{rms}}(N_{\text{star}}) = 0.001 \times \sqrt{N_{\text{star}}/1000}. \quad (3.25)$$

This relation is a consequence of the weak signal limit which holds approximately in this particular case, with the approximation getting better and better on increasing the overall noise level. We verified that eq. (3.25) holds for a reasonable number of stars – but can not do so for a number of stars beyond $N_{\text{star}} \gtrsim 5000$, due to the increasing computational costs involved. (But see below for a method to handle such situations.) With $N_{\text{star}} = 10^5$, relation (3.25) gives a noise level of $\Delta\theta_{\text{rms}} = 0.01$ milli-arcseconds (mas).

We proceed presenting two more examples, plotted in Figure 8, denoted with **Case 2** and **3**. They represent a case where the overall noise level for astrometry (σ^2) is reduced by a factor of 2 (Figure 8 left panel), and a situation keeping the same noise properties for the astrometry set, but with the PTA system in the strong-signal (noiseless) regime (Figure 8 right panel). The astrometric data alone do not set meaningful constraints on the SGWB properties: however, they are still able to improve the constraining power of the PTA data exploiting cross-correlations among data sets. The improvement can be significant if the PTA datasets are not in the strong signal regime; however, it is much smaller if that is indeed the case.

3.2.2 A method for handling large Fisher matrices

In the examples discussed above we are able to perform the necessary computations involving Fisher matrices and their inversion, given the relatively small size of astrometric covariance

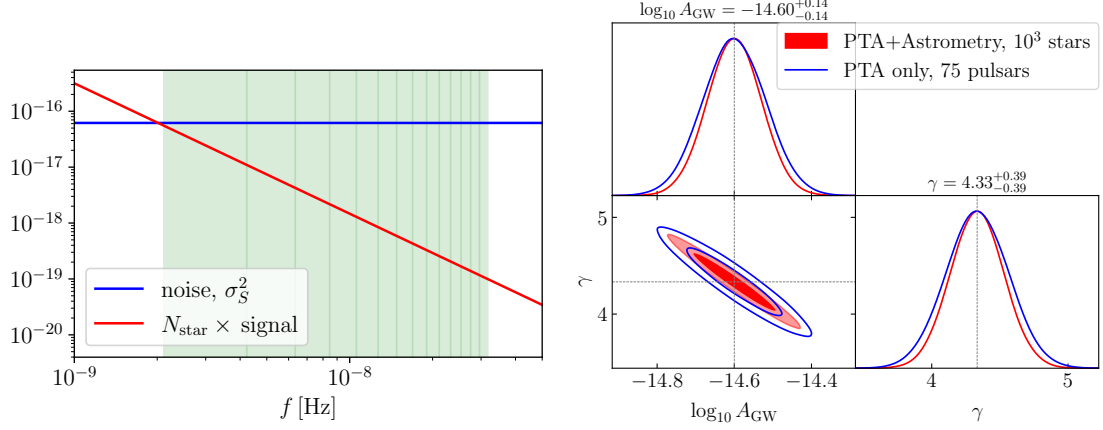


Figure 7: Noise vs signal (**left**) + Fisher forecast (**right**) for the Case 1 example of section 3.2.1. Limits are 95% C.L and correspond to the joint PTA+Astrometric forecast.

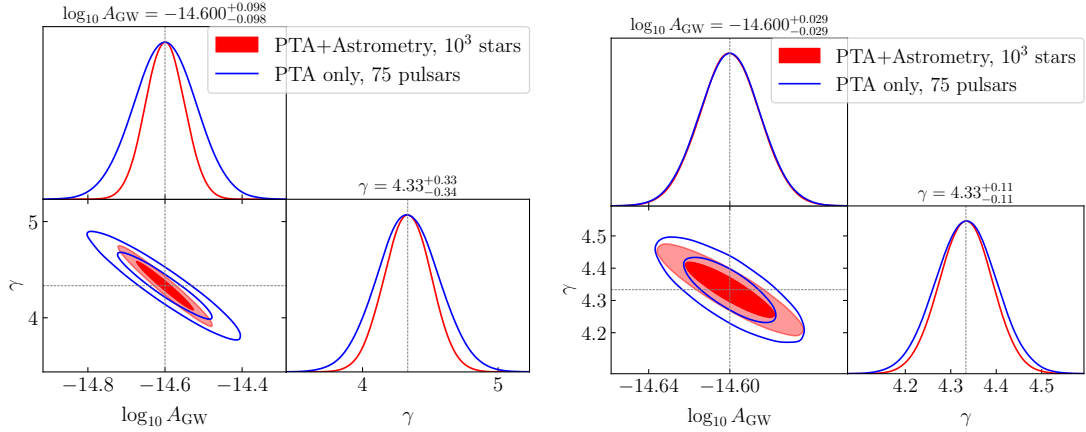


Figure 8: Fisher forecast for the lower astrometric noise level with same PTA noise as above (**left**) and noiseless PTA (**right**). These are Case 2 and 3 examples of section 3.2.1. Limits are 95% C.L and correspond to the joint PTA+Astrometric forecast.

matrix involved. However, for realistic datasets which may contain over 10^6 stars, inverting matrices of such dimensionality can become demanding. To handle forecasts for such datasets, we develop a simple method to perform the Fisher forecasts in weak astrometric signal limit without needing to resort to the full numerical calculations. The weak signal limit is justified since current astrometric datasets are very much in the noise dominated regime and this is likely to be the case in the future as well.¹¹ Thus, we can approximate the matrix D of equation (3.20) as

$$D_{ij} \approx \delta_{ij} \sigma_i^2, \quad [D^{-1}]_{ij} = \delta_{ij} \sigma_i^{-2}. \quad (3.26)$$

We further assume all stars to have the same measurement noise $\sigma_i^2 = \sigma_S^2$, as well as identical noise for each pulsar σ_p^2 .

In the noise dominated approximation for the astrometric covariance, we write

$$C^{-1} = \begin{bmatrix} (A - B\sigma_S^{-2}\mathbb{1}_M B^T)^{-1} & 0 \\ 0 & (\sigma_S^2\mathbb{1}_M - B^T A^{-1} B)^{-1} \end{bmatrix} \begin{bmatrix} \mathbb{1}_N & -B\sigma_S^{-2}\mathbb{1}_M \\ -B^T A^{-1} & \mathbb{1}_M \end{bmatrix}. \quad (3.27)$$

Note that we do not assume a weak signal limit for the pulsar covariance: in fact, we work with the full PTA covariance matrix. In fact, we focus on the relevant regime for PTA experiments, since current measurements already suggest PTA measurements to lie in the intermediate signal regime – especially for the lower end of the frequency range. To evaluate the trace we compute

$$\begin{aligned} C_\alpha C^{-1} &= \begin{bmatrix} A_\alpha Q_1 & B_\alpha Q_2 \\ B_\alpha^T Q_1 & D_\alpha Q_2 \end{bmatrix} \begin{bmatrix} \mathbb{1}_N & -B\sigma_S^{-2}\mathbb{1}_M \\ -B^T A^{-1} & \mathbb{1}_M \end{bmatrix}, \\ &= \begin{bmatrix} A_\alpha Q_1 - B_\alpha Q_2 B^T A^{-1} & -\sigma_S^{-2} A_\alpha Q_1 B + B_\alpha Q_2 \\ B_\alpha^T Q_1 - D_\alpha Q_2 B^T A^{-1} & -\sigma_S^{-2} B_\alpha^T Q_1 B + D_\alpha Q_2 \end{bmatrix}. \end{aligned} \quad (3.28)$$

where

$$Q_1 = (A - B\sigma_S^{-2}\mathbb{1}_M B^T)^{-1}, \quad (3.29)$$

$$Q_2 = \sigma_S^{-2} (\mathbb{1}_M - \sigma_S^{-2} B^T A^{-1} B)^{-1}. \quad (3.30)$$

To proceed, we first note some useful relations involving the inverse of matrices

$$(A - B\frac{\mathbb{1}_M}{\sigma_S^2} B^T)^{-1} \approx \left[\mathbb{1}_N + \frac{A^{-1} B B^T}{\sigma_S^2} + \mathcal{O}(1/\sigma_S^4) \right] A^{-1}, \quad (3.31)$$

$$(D - B^T A^{-1} B)^{-1} \approx \frac{1}{\sigma_S^2} \left[\mathbb{1}_M + \frac{B^T A^{-1} B}{\sigma_S^2} + \mathcal{O}(1/\sigma_S^4) \right]. \quad (3.32)$$

¹¹To be precise this requires $MI(f) \ll \sigma^2(f)$ where σ^2 denotes the frequency domain noise power spectral density. This condition ensures that the effect of the off-diagonal terms in the covariance is suppressed compared to the diagonal terms.

Then, we define $C_\alpha C^{-1} \equiv \mathcal{M}_\alpha$. For computing the trace in the expressions above, we need the diagonal elements of $\mathcal{M}_\alpha \mathcal{M}_\beta \equiv C_\alpha C^{-1} C_\beta C^{-1}$

$$\mathcal{F}_{\alpha\beta} = \frac{1}{2} \text{Tr}[\mathcal{M}_\alpha \mathcal{M}_\beta] = \frac{1}{2} \left\{ \underbrace{\text{Tr}[\mathcal{M}_{\alpha,11} \mathcal{M}_{\beta,11}]}_{\mathcal{O}(1)} + \underbrace{\text{Tr}[\mathcal{M}_{\alpha,12} \mathcal{M}_{\beta,21}]}_{\mathcal{O}(1/\sigma_S^2)} \right. \\ \left. + \underbrace{\text{Tr}[\mathcal{M}_{\alpha,21} \mathcal{M}_{\beta,12}]}_{\mathcal{O}(1/\sigma_S^2)} + \underbrace{\text{Tr}[\mathcal{M}_{\alpha,22} \mathcal{M}_{\beta,22}]}_{\mathcal{O}(1/\sigma_S^4)} \right\}. \quad (3.33)$$

In the above equation the, term in the right-hand-side of the first line denotes the upper left $N \times N$ block of $\mathcal{M}_\alpha \mathcal{M}_\beta$ and the term in the second line denotes the lower right $M \times M$ block (with N and M controlling respectively the pulsar and star numbers). We explicitly indicate the order of the expansion in the small $1/\sigma_S^2$ parameter.

In fact, working in a noise-dominated, large σ_S regime for astrometry, we write – up to first order in σ_S^{-2} :

$$\mathcal{M}_\alpha = \mathcal{M}_\alpha^{(0)} + \sigma_S^{-2} \mathcal{M}_\alpha^{(1)}, \quad (3.34)$$

with

$$\mathcal{M}_\alpha^{(0)} = \begin{bmatrix} A_\alpha A^{-1} & 0 \\ B_\alpha^T A^{-1} & 0 \end{bmatrix}, \quad (3.35)$$

$$\mathcal{M}_\alpha^{(1)} = \begin{bmatrix} A_\alpha A^{-1} B B^T A^{-1} - B_\alpha B^T A^{-1} & B_\alpha - A_\alpha A^{-1} B \\ B_\alpha^T A^{-1} B B^T A^{-1} - D_\alpha B^T A^{-1} & D_\alpha - B_\alpha^T A^{-1} B \end{bmatrix}. \quad (3.36)$$

Explicitly, an expansion of the Fisher matrix up to order $1/\sigma_S^2$ gives the formula

$$\mathcal{F}_{\alpha\beta} = \frac{1}{2} \text{Tr}[\mathcal{M}_\alpha^{(0)} \mathcal{M}_\beta^{(0)}] + \frac{1}{2\sigma_S^2} \text{Tr}[\mathcal{M}_\alpha^{(0)} \mathcal{M}_\beta^{(1)} + \mathcal{M}_\alpha^{(1)} \mathcal{M}_\beta^{(0)}] \\ = \frac{1}{2} \text{Tr}[A_\alpha A^{-1} A_\beta A^{-1}] \\ + \frac{1}{2\sigma_S^2} \text{Tr}[A_\alpha A^{-1} A_\beta A^{-1} B B^T A^{-1} - A_\alpha A^{-1} B_\beta B^T A^{-1} - A_\alpha A^{-1} B B_\beta^T A^{-1}] \\ + \frac{1}{2\sigma_S^2} \text{Tr}[A_\alpha A^{-1} B B^T A^{-1} A_\beta A^{-1} - B_\alpha B^T A^{-1} A_\beta A^{-1} - B_\alpha^T A^{-1} A_\beta A^{-1} B] \\ + \frac{1}{2\sigma_S^2} \text{Tr}[B_\alpha^T A^{-1} B_\beta + B_\alpha B_\beta^T A^{-1}]. \quad (3.38)$$

At zeroth order in $1/\sigma_S^2$, we recover the PTA only Fisher matrix – first line of eq. (3.38). At order $\mathcal{O}(1/\sigma_S^2)$ we obtain the first corrections to the PTA-only forecasts, associated with synergies with astrometry. Since the relevant terms always include the matrix B , such corrections include the pulsar-star correlations. Notice that this perturbative expansion of the Fisher matrix greatly simplifies the numerical calculations in the astrometric noise dominated regime, since we only

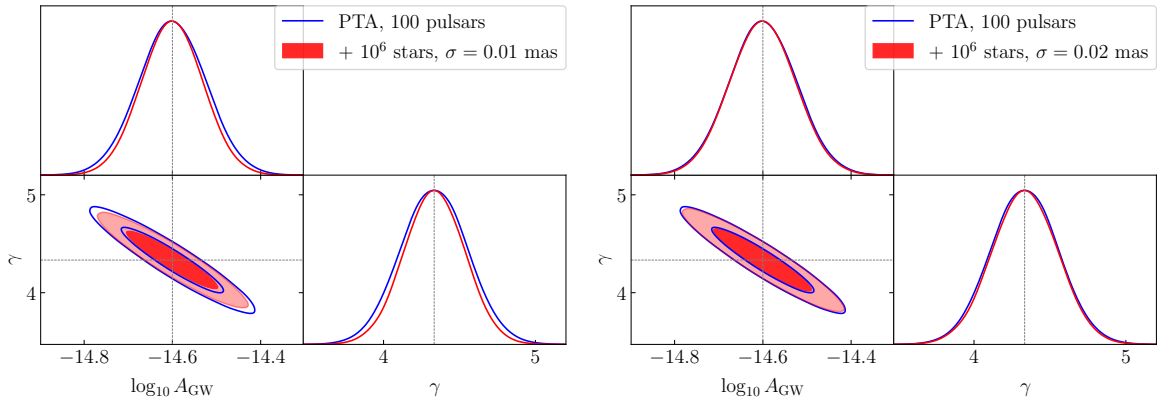


Figure 9: Fisher forecast for the amplitude and slope of the SGWB for a fiducial value $\log_{10} A_{\text{GW}} = -14.6$, $\gamma = 13/3$. In red, the PTA only case with the number of pulsars and noise parameters chosen to match the sensitivity of the combined IPTA dataset [9]. In blue, the forecasts on the addition of PTA–Astrometry cross-correlations with 10^6 stars. **Left:** astrometry noise $\sigma = 0.01$ mas. **Right:** astrometry noise $\sigma = 0.02$ mas.

	$\log A_{\text{GW}}$	γ
PTA only	-14.6 ± 0.076	$13/3 \pm 0.22$
PTA + Astrometry, $\sigma = 0.01$ mas	-14.6 ± 0.069	$13/3 \pm 0.19$
PTA + Astrometry, $\sigma = 0.02$ mas	-14.6 ± 0.074	$13/3 \pm 0.21$

Table 1: Fiducial parameter values and marginalised 1σ limits from the Fisher forecast. We focus on synergy measurements of the SGWB monopole as discussed in section 3.2.2.

have to deal with matrices of size $N \times N$ and $N \times M$, but not $M \times M$ where M can be of the order 10^5 or larger. (Recall that N is the number of pulsars, M is twice the number of stars which are monitored.) On the other hand for typical pulsar datasets, currently and in the near future we have to handle matrices of size $N \sim \mathcal{O}(100)$, which is manageable with standard computing resources.

We then use this approach to compute the full Fisher matrix, combining the individual per-frequency Fisher matrices. In Fig. 9, we present our results for a PTA setup with 75 pulsars and an astrometric setup with 10^6 stars. The astrometric setup has $\Delta\theta_{\text{rms}} = 0.01$ mas and $T_{\text{cad}} = \text{year}/15$, i.e. roughly corresponding to the observational cadence of Gaia. Our results indicate that for the case with $\sigma = 0.01$ mas, we obtain roughly a 10% improvement over the PTA-only constraints, while for $\sigma \geq 0.02$ mas, the improvement will be negligible.¹² See Table 1 for the exact numbers.

¹²We note that for the $\sigma = 0.01$ mas, the weak signal limit does not hold for the first frequency bin where the signal and noise are comparable in magnitude. However, our results from section 3.2.1 indicate that our perturbative expansion for the Fisher matrix may even underestimate the improvement compared to the full calculation (see fig. 8).

3.2.3 The case of dipolar anisotropy

We conclude our analysis with a discussion of the prospects to detect a possible SGWB dipolar anisotropy through the synergy of astrometry and PTA. We aim to quantify the minimal level of anisotropy detectable by perspective PTA-only data, and with the joint system astrometry-PTA using the same configurations used in the previous section. Although our analysis is tailored to the kinematic dipole (see eq. (2.7)), we expect that similar considerations hold for the case of dipolar statistical anisotropies, of which the kinematic dipole is just a specific case. Given the crucial role that anisotropies may play in distinguishing astrophysical versus cosmological sources of SGWB, such a question is important to address. Notice that current upper limits on the magnitude of SGWB anisotropies lie at 10% level relative to monopole [66, 101].

We carry on the analysis with the same approach developed in section 3.2. The components A , B , D entering in the covariance matrix (3.16) now read

$$A_{pq} = \frac{(\gamma_{pq}^{(0)} + \gamma_{pq}^{(1)})I_f}{(4\pi f)^2} + \sigma_p^2 \delta_{pq}, \quad (3.39)$$

$$B_{pa} = \frac{(K_{p,a}^{(0)} + K_{p,a}^{(1)})I_f}{4\pi f}, \quad (3.40)$$

$$D_{ab} = (H_{ab}^{(0)} + H_{ab}^{(1)})I_f + \delta_{ab}\sigma_a^2. \quad (3.41)$$

Besides the monopole, we now include the contributions to the dipole ORF: $\gamma^{(1)}$ for PTA [71], $K^{(1)}$ for the cross-correlation and astrometry-only $H^{(1)}$ (see section 2). The analysis proceeds in the same manner as the previous section and the results are plotted in Fig. 10. The fiducial parameter means and the marginalised 1σ Fisher errors are collected in Table 2.

	$\log A_{\text{GW}}$	γ	β
PTA only	-14.6 ± 0.076	$13/3 \pm 0.22$	0.05 ± 0.07
PTA + Astrometry, $\sigma = 0.01$ mas	-14.6 ± 0.069	$13/3 \pm 0.19$	0.05 ± 0.029
PTA + Astrometry, $\sigma = 0.02$ mas	-14.6 ± 0.074	$13/3 \pm 0.21$	0.05 ± 0.047

Table 2: Fiducial parameter values and marginalised 1σ limits from the Fisher forecast. In this Table we report limits on the size of dipolar anisotropy, as discussed in section 3.2.3.

We choose the same fiducial A_{GW} and γ as in section 3.2.1. We select a level of dipole anisotropy $\beta = 5 \times 10^{-2}$, finding this value to be the minimum level of kinematic dipole that will be detectable with our PTA + Astrometry setup. Thus, astrometry can again help to tighten the constraints on the dipole anisotropy, which can be useful in determining the origin of the SGWB. Reaching the kinematic dipole level with PTA alone requires a substantial increase in the number of pulsars ($N > 1000$) [88, 101] which may only be achievable with SKA. It would be also interesting to explore how cross-correlations with astrometric datasets could work to improve SGWB sensitivity in the SKA-era.

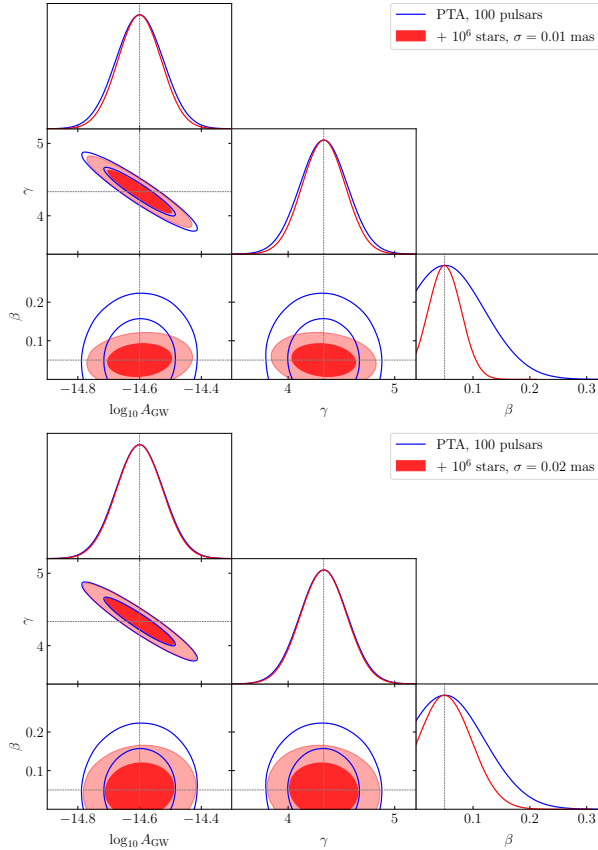


Figure 10: Fisher forecast for the SGWB parameters, with the addition of the dipole.

4 Conclusions

In the next few years, evidence for the SGWB in the nHz range is likely to grow as PTA experiments collect more and more data. We can expect an increased statistical significance for the Hellings-Downs correlation, as well as tighter constraints on the amplitude and frequency spectrum of the SGWB. The next generation of radio telescopes – SKA is expected to begin operations in the early 2030s and is projected to observe a large number of pulsars with unprecedented timing precision [15], possibly leading to precise determination of the SGWB parameters. A complementary probe of the nHz SGWB is provided by astrometry – corresponding to the precise monitoring of the positions of a large number of stars. Data from astrometric surveys such as Gaia, has already been used to constrain SGWB in the frequency range $f \lesssim 10^{-9}$ Hz [40–43]. In this work, we have considered how astrometry data in the nHz band will complement PTA observations, and how it can be used to characterize the properties of SGWB beyond what can be obtained from PTA-only data.

In section 2, we first reviewed the theory behind the astrometric detection of SGWB and derived for the first time fully covariant, analytical expressions for the kinematic dipole ORFs of the auto-correlation of the astrometric deflections, as well as their cross-correlation with pulsar timing residuals. Our expressions allowed us to manifestly visualise the sensitivity of the astrometric and PTA setups to the SGWB properties, as a function of the locations of monitored

objects.

In section 3 we studied the sensitivity of the astrometric and PTA setups to the SGWB, focusing on the measurement of the SGWB amplitude, spectral tilt and the magnitude of the kinematic dipole anisotropy. In section 3.1 we derived optimal estimators for SGWB monopole and dipole measurements in this context, built in terms of quadratic combinations of the astrometric deflections. We used these formulas to forecast the sensitivity of astrometry to the SGWB monopole and dipole, assuming a large number of stars uniformly distributed across the sky. In section 3.2, we analysed the joint PTA-Astrometry setup and showed that cross-correlating PTA and Astrometry data could tighten the constraints on SGWB obtained from PTA data alone. We used Fisher forecasts to calculate the sensitivity to the SGWB amplitude, spectral shape and dipole, finding that an astrometric survey with 0.01 mas astrometric precision and the typical number of sources and cadence of Gaia could lead to noticeable improvements over current PTA only SGWB constraints. Improvements on the PTA constraints can be quite useful, since tighter constraints on the SGWB parameters can be used to rule out models and potentially distinguish between and astrophysical or cosmological signal.

The flood of upcoming data from PTA and astrometry experiments presents both challenges and opportunities. The possibility of a joint PTA-astrometry data analysis will hold exciting potential since cross-correlations between timing residuals and astrometric deflections could be leveraged to deliver tighter SGWB constraints compared to either of the experiments alone. Thus, developing efficient implementations of joint PTA-astrometry analysis will be crucial for harnessing the power of these cross-correlations. It would also be interesting to further explore such synergies in the context of general SGWB anisotropies and study their detectability. We leave such pursuits to future work.

Acknowledgements

We are partially funded by the STFC grants ST/T000813/1 and ST/X000648/1. We also acknowledge the support of the Supercomputing Wales project, which is part-funded by the European Regional Development Fund (ERDF) via Welsh Government. We acknowledge the use of the `GetDist` software package for visualising the results of the Fisher forecasts [106]. For the purpose of open access, the authors have applied a Creative Commons Attribution licence to any Author Accepted Manuscript version arising.

A Spectrum of angular deflection fluctuations

In this Appendix we make use of our analytical, covariant expressions for the ORF to show that dipolar anisotropies induce correlations between electric and magnetic components of star deflections. We use the notation of [25], to which we refer the reader for more details on the nomenclature.

The EB correlation will be given by

$$C_{Elm B'l'm'} = \frac{1}{\ell(\ell+1)} \int d^2\Omega_n d^2\Omega_{n'} Y_{lm}^*(n) Y_{l'm'}(n') \beta(4 - n_\Omega) \beta^{EB}, \quad (\text{A.1})$$

where

$$\beta^{EB} = \nabla_i \nabla'_b \left[\varepsilon_{jab} n_a H_{ij}^{(1)} \right]. \quad (\text{A.2})$$

Where ∇_i and ∇'_b are normal 3D derivatives with respect to \mathbf{z} and \mathbf{z}' with $\mathbf{n} = \mathbf{z}/|\mathbf{z}|$, $\mathbf{q} = \mathbf{z}'/|\mathbf{z}'|$. Now, we only need to focus on the parts of $H_{ij}^{(1)}$ (see (2.15)), which are not invariant under $\mathbf{n} \rightarrow -\mathbf{n}$ and $\mathbf{q} \rightarrow -\mathbf{q}$, as these give a zero contribution [25]. Thus, we only have the following contribution:

$$\begin{aligned} \beta^{EB} &= \nabla_i \nabla'_b \left[a_1 \varepsilon_{jab} n_a \left(\varepsilon^{ilm} n_l q_m [(\mathbf{n} \cdot \mathbf{q}) q^j - n^j] + \varepsilon^{jlm} n_l q_m [(\mathbf{n} \cdot \mathbf{q}) n^i - q^i] \right) \right] \\ &= \nabla_i \nabla'_b \left[a_1 T^{bi} \right], \end{aligned} \quad (\text{A.3})$$

where

$$T^{bi} = (q^b - (\mathbf{n} \cdot \mathbf{q}) n^b) (q^i + n^i) ((\mathbf{n} \cdot \mathbf{q}) - 1) - (n^i q^b - (\mathbf{n} \cdot \mathbf{q}) \delta^{ib}) ((\mathbf{n} \cdot \mathbf{q})^2 - 1), \quad (\text{A.4a})$$

and a_1 is defined in (2.17),

So we need $\nabla_i X$, $\nabla'_b X$, $\nabla_i \nabla'_b X$, where $X = a_1, T^{bi}$. We can use the relations $\nabla_i n_j = \delta_{ij} - n_i n_j$, $\nabla'_i q_j = \delta_{ij} - q_i q_j$, $\nabla_i q_j = \nabla'_i n_j = \nabla_i v_j = \nabla'_i v_j = 0$, as well as

$$\nabla_i (\mathbf{n} \cdot \mathbf{q}) = q_i - (\mathbf{n} \cdot \mathbf{q}) n_i, \quad \nabla'_b (\mathbf{n} \cdot \mathbf{q}) = n_b - (\mathbf{n} \cdot \mathbf{q}) q_b. \quad (\text{A.5})$$

Using these, we find:

$$\nabla_i \nabla'_b (a_1) T^{bi} = -\frac{\pi}{12} \varepsilon^{ljk} v_l n_j q_k F_1 \left[2 - \left(-3 + \frac{F_{1,y}}{F_1} (\mathbf{n} \cdot \mathbf{q} - 1) - 2 \mathbf{n} \cdot \mathbf{q} \right) (\mathbf{n} \cdot \mathbf{q})^2 (\mathbf{n} \cdot \mathbf{q} - 1) \right], \quad (\text{A.6a})$$

$$\nabla_i (a_1) \nabla'_b (T^{bi}) = -\frac{\pi}{12} \varepsilon^{ljk} v_l n_j q_k F_1 (1 - \mathbf{n} \cdot \mathbf{q}) [-1 + (\mathbf{n} \cdot \mathbf{q})^2 (\mathbf{n} \cdot \mathbf{q} (\mathbf{n} \cdot \mathbf{q} - 7) - 1)], \quad (\text{A.6b})$$

$$\nabla'_b (a_1) \nabla_i (T^{bi}) = -\frac{\pi}{6} \varepsilon^{ljk} v_l n_j q_k (1 + \mathbf{n} \cdot \mathbf{q} + (\mathbf{n} \cdot \mathbf{q})^2 (2 + \mathbf{n} \cdot \mathbf{q})) \left(F_2 \mathbf{n} \cdot \mathbf{q} + \frac{F_1}{2} (1 - (\mathbf{n} \cdot \mathbf{q})^2) \right), \quad (\text{A.6c})$$

$$(a_1) \nabla_i \nabla'_b (T^{bi}) = \frac{\pi}{6} \varepsilon^{ljk} v_l n_j q_k F_2 [1 - \mathbf{n} \cdot \mathbf{q} (2 + \mathbf{n} \cdot \mathbf{q} [4 + \mathbf{n} \cdot \mathbf{q} (3 \mathbf{n} \cdot \mathbf{q} - 10)])], \quad (\text{A.6d})$$

where we defined

$$F_1 = \frac{(-1 + 4y - 14y^2 + 11y^3 - 3y^2(2y + 1) \ln(y))}{(y^2(1 - y)^4)}, \quad (\text{A.7})$$

$$F_2 = \frac{\left(1 - 4y - \frac{3y^2 \ln(y)}{(1-y)} \right)}{y(1 - y)^2}, \quad (\text{A.8})$$

to simplify notation and $F_{1,y} = dF_1/dy$. Combining and simplifying these, we get for (A.3):

$$\beta^{EB} = \frac{\pi}{12} \mathbf{v} \cdot (\mathbf{n} \times \mathbf{q}) G(y), \quad (\text{A.9})$$

where

$$G(y) = -\frac{2}{y^2(y-1)^5} \left[(y-1)(-1+6y-42y^2+170y^3-481y^4+800y^5-684y^6+208y^7+96y^8) - 3y^2(-1-y+13y^2-77y^3+198y^4-236y^5+128y^6) \ln(y) \right], \quad (\text{A.10})$$

where y is defined in eq. (2.12). Note that β^{EB} depends on the angles between \mathbf{v} with \mathbf{n} and \mathbf{q} as well as ζ .

B Angular dependence of overlap reduction functions

In this Appendix we report explicit formulas for the traces of matrix combinations used in section 2 for representing the sensitivity of the PTA and astrometry system to the properties of SGWB. From equations (2.13) and (2.24)

$$\text{Tr}[\mathbf{H}_0 \mathbf{H}_0] = \frac{\pi^2 (\cos^2(\zeta) + 1)}{9(\cos(\zeta) + 1)^2} \times \quad (\text{B.1})$$

$$\left(-7 \cos^2(\zeta) - 2 \cos(\zeta) + 6(\cos(\zeta) - 1)^2 \ln \left(\sin^2 \left(\frac{\zeta}{2} \right) \right) + 5 \right)^2$$

$$\mathbf{K}_0 \mathbf{K}_0^T = \frac{16}{9} \pi^2 \tan^2 \left(\frac{\zeta_{sp}}{2} \right) \times \quad (\text{B.2})$$

$$\left(-3 \ln(1 - \cos(\zeta_{sp})) + \cos(\zeta_{sp}) \left(3 \ln \left(\sin^2 \left(\frac{\zeta_{sp}}{2} \right) \right) - 2 \right) - 2 + \ln(8) \right)^2,$$

where ζ is the angle between the stars at directions \mathbf{n} and \mathbf{q} , while ζ_{sp} is the angle between a star in direction \mathbf{n} and a pulsar at direction \mathbf{x} .

With equations (2.15) and (2.27) we get

$$\text{Tr}[\mathbf{H}_1 \mathbf{H}_1] = \frac{64\pi^2 (\alpha_H (Av)^2 \sqrt{1-y} y^2 + 4\delta_H^2 (y-1)y^4 (\beta_H - \gamma_H \sqrt{1-y}))}{9((nq)^2 - 1)^2 (1-y)^{5/2}} \quad (\text{B.3})$$

$$\mathbf{K}_1 \mathbf{K}_1^T = \frac{4\pi^2 (nx^2 - 1) ((nx+1)^2 (\alpha_K \beta_K^2 - (A_1 v)^4 (5 - 6nx)^2) + 12\gamma_K \ln(\frac{1-nx}{2}))}{9(nx+1)^4 ((A_1 v) - (A_1 v)nx)^2}, \quad (\text{B.4})$$

where

$$\alpha_H = -(y-1)^2 (nq^2 y^2 (2y+1)^2 + 2nq(1-4y)^2 + y^2 (2y+1)^2) + \quad (\text{B.5})$$

$$6(y-1)y^2 (2(nq^2+1)y^2 + nq(nq+8)y - 2nq + y) \ln(y) - 9(nq+1)^2 y^4 \ln^2(y)$$

$$\beta_H = (nq)^2 (nv)(y-1) \sqrt{\frac{(Av)^2}{y-1} + 4((nv)^2 - 1)y} \quad (\text{B.6})$$

$$-(nv) \sqrt{1-y} \sqrt{4((nv)^2 - 1)(y-1)y - (Av)^2}$$

$$\gamma_H = (nv)^2 ((nq)^2 - 2y + 1) + (nq)^2 (-y) + y \quad (\text{B.7})$$

$$\delta_H = 1 + y - 2y^2 + 3y \ln y, \quad (\text{B.8})$$

and

$$\alpha_K = -1 + (nv)^2 + (nx)^2 - 2nv(nx)(vx) + (vx)^2 \quad (\text{B.9})$$

$$\beta_K = nv(4 + nx(-7 + 2nx)) + (4 + 3(-2 + nx)nx)vx \quad (\text{B.10})$$

$$\begin{aligned} \gamma_K = & (-1 + nx)^2(1 + nx)((A_1v)^4(-5 + 6nx) + (nv + vx)\alpha_K\beta_K) + \\ & 3(-1 + nx)^4(-(A_1v)^4 + (nv + vx)^2\alpha_K) \ln\left(\frac{1 - nx}{2}\right). \end{aligned} \quad (\text{B.11})$$

When the vector \mathbf{n} is parallel to \mathbf{v} , then $Av = 0$ and equation (B.3) is simpler. For this case $\mathbf{K}_1\mathbf{K}_1^T$ is calculated with (2.28). More specifically when $\mathbf{n} = -\mathbf{v}$, we get

$$\text{Tr}[\mathbf{H}_1\mathbf{H}_1] = \frac{4\pi^2(\cos(\zeta) - 1)^2(\cos^2(\zeta) + 1)}{9(\cos(\zeta) + 1)^2} \times \quad (\text{B.12})$$

$$\begin{aligned} & (\cos^2(\zeta) - \cos(\zeta) - \ln(8)\cos(\zeta) + 3(\cos(\zeta) - 1)\ln(1 - \cos(\zeta)) - 2 + \ln(8))^2 \\ \mathbf{K}_1\mathbf{K}_1^T = & \frac{1}{9}\pi^2 \tan^2\left(\frac{\zeta_{sp}}{2}\right) \times \quad (\text{B.13}) \\ & \left(2\cos(\zeta_{sp}) - 3\cos(2\zeta_{sp}) - 12(\cos(\zeta_{sp}) - 1)\ln\left(\sin^2\left(\frac{\zeta_{sp}}{2}\right)\right) + 5\right)^2. \end{aligned}$$

Similar expressions for the case $\mathbf{n} = \mathbf{v}$.

References

- [1] **NANOGrav** Collaboration, Z. Arzoumanian et al., “The NANOGrav 12.5 yr Data Set: Search for an Isotropic Stochastic Gravitational-wave Background,” *Astrophys. J. Lett.* **905** no. 2, (2020) L34, [arXiv:2009.04496](#) [[astro-ph.HE](#)].
- [2] B. Goncharov et al., “On the Evidence for a Common-spectrum Process in the Search for the Nanohertz Gravitational-wave Background with the Parkes Pulsar Timing Array,” *Astrophys. J. Lett.* **917** no. 2, (2021) L19, [arXiv:2107.12112](#) [[astro-ph.HE](#)].
- [3] **EPTA** Collaboration, S. Chen et al., “Common-red-signal analysis with 24-yr high-precision timing of the European Pulsar Timing Array: inferences in the stochastic gravitational-wave background search,” *Mon. Not. Roy. Astron. Soc.* **508** no. 4, (2021) 4970–4993, [arXiv:2110.13184](#) [[astro-ph.HE](#)].
- [4] J. Antoniadis et al., “The International Pulsar Timing Array second data release: Search for an isotropic gravitational wave background,” *Mon. Not. Roy. Astron. Soc.* **510** no. 4, (2022) 4873–4887, [arXiv:2201.03980](#) [[astro-ph.HE](#)].
- [5] **NANOGrav** Collaboration, G. Agazie et al., “The NANOGrav 15 yr Data Set: Evidence for a Gravitational-wave Background,” *Astrophys. J. Lett.* **951** no. 1, (2023) L8, [arXiv:2306.16213](#) [[astro-ph.HE](#)].
- [6] **EPTA, InPTA:** Collaboration, J. Antoniadis et al., “The second data release from the European Pulsar Timing Array - III. Search for gravitational wave signals,” *Astron. Astrophys.* **678** (6, 2023) A50, [arXiv:2306.16214](#) [[astro-ph.HE](#)].
- [7] D. J. Reardon et al., “Search for an Isotropic Gravitational-wave Background with the Parkes Pulsar Timing Array,” *Astrophys. J. Lett.* **951** no. 1, (2023) L6, [arXiv:2306.16215](#) [[astro-ph.HE](#)].

- [8] H. Xu *et al.*, “Searching for the Nano-Hertz Stochastic Gravitational Wave Background with the Chinese Pulsar Timing Array Data Release I,” [Res. Astron. Astrophys.](#) **23** no. 7, (2023) 075024, [arXiv:2306.16216 \[astro-ph.HE\]](#).
- [9] **International Pulsar Timing Array** Collaboration, G. Agazie *et al.*, “Comparing recent PTA results on the nanohertz stochastic gravitational wave background,” [arXiv:2309.00693 \[astro-ph.HE\]](#).
- [10] M. T. Miles *et al.*, “The MeerKAT Pulsar Timing Array: The first search for gravitational waves with the MeerKAT radio telescope,” [arXiv:2412.01153 \[astro-ph.HE\]](#).
- [11] R. W. Hellings and G. S. Downs, “Upper limits on the isotropic gravitational radiation background from pulsar timing analysis,” [Astrophys. J. Lett.](#) **265** (Feb., 1983) L39–L42.
- [12] A. Sesana, A. Vecchio, and C. N. Colacino, “The stochastic gravitational-wave background from massive black hole binary systems: implications for observations with Pulsar Timing Arrays,” [Mon. Not. Roy. Astron. Soc.](#) **390** (2008) 192, [arXiv:0804.4476 \[astro-ph\]](#).
- [13] S. Burke-Spolaor *et al.*, “The Astrophysics of Nanohertz Gravitational Waves,” [Astron. Astrophys. Rev.](#) **27** no. 1, (2019) 5, [arXiv:1811.08826 \[astro-ph.HE\]](#).
- [14] C. Caprini and D. G. Figueroa, “Cosmological Backgrounds of Gravitational Waves,” [Class. Quant. Grav.](#) **35** no. 16, (Aug., 2018) 163001, [arXiv:1801.04268 \[astro-ph.CO\]](#).
<https://iopscience.iop.org/article/10.1088/1361-6382/aac608>.
- [15] G. Janssen *et al.*, “Gravitational wave astronomy with the SKA,” [PoS AASKA14](#) (2015) 037, [arXiv:1501.00127 \[astro-ph.IM\]](#).
- [16] E. F. Keane *et al.*, “A Cosmic Census of Radio Pulsars with the SKA,” [PoS AASKA14](#) (2015) 040, [arXiv:1501.00056 \[astro-ph.IM\]](#).
- [17] E. V. Linder, “Relativistic scattering coherence,” [Phys. Rev. D](#) **34** (Sep, 1986) 1759–1763.
<https://link.aps.org/doi/10.1103/PhysRevD.34.1759>.
- [18] V. B. Braginsky, N. S. Kardashev, I. D. Novikov, and A. G. Polnarev, “Propagation of electromagnetic radiation in a random field of gravitational waves and space radio interferometry,” [Nuovo Cim. B](#) **105** (1990) 1141–1158.
- [19] R. Fakir, “Gravity Wave Watching,” [Astrophysical Journal](#) **426** (May, 1994) 74, [arXiv:gr-qc/9304003 \[gr-qc\]](#).
- [20] T. Pyne, C. R. Gwinn, M. Birkinshaw, T. M. Eubanks, and D. N. Matsakis, “Gravitational radiation and very long baseline interferometry,” [Astrophys. J.](#) **465** (1996) 566–577, [arXiv:astro-ph/9507030](#).
- [21] N. Kaiser and A. H. Jaffe, “Bending of light by gravity waves,” [Astrophys. J.](#) **484** (1997) 545–554, [arXiv:astro-ph/9609043](#).
- [22] C. R. Gwinn, T. M. Eubanks, T. Pyne, M. Birkinshaw, and D. N. Matsakis, “Quasar proper motions and low frequency gravitational waves,” [Astrophys. J.](#) **485** (1997) 87–91, [arXiv:astro-ph/9610086](#).
- [23] S. M. Kopeikin, G. Schaefer, C. R. Gwinn, and T. M. Eubanks, “Astrometric and timing effects of gravitational waves from localized sources,” [Phys. Rev. D](#) **59** (1999) 084023, [arXiv:gr-qc/9811003](#).
- [24] B. F. Schutz, “Astrometric and timing effects of gravitational waves,” [Proceedings of the International Astronomical Union](#) **5** no. S261, (2009) 234–239.
- [25] L. G. Book and E. E. Flanagan, “Astrometric Effects of a Stochastic Gravitational Wave Background,” [Phys. Rev. D](#) **83** (2011) 024024, [arXiv:1009.4192 \[astro-ph.CO\]](#).

- [26] C. J. Moore, D. P. Mihaylov, A. Lasenby, and G. Gilmore, “Astrometric Search Method for Individually Resolvable Gravitational Wave Sources with Gaia,” *Phys. Rev. Lett.* **119** no. 26, (2017) 261102, [arXiv:1707.06239](#) [[astro-ph.IM](#)].
- [27] S. A. Klioner, “Gaia-like astrometry and gravitational waves,” *Class. Quant. Grav.* **35** no. 4, (2018) 045005, [arXiv:1710.11474](#) [[astro-ph.HE](#)].
- [28] D. P. Mihaylov, C. J. Moore, J. R. Gair, A. Lasenby, and G. Gilmore, “Astrometric Effects of Gravitational Wave Backgrounds with non-Einsteinian Polarizations,” *Phys. Rev. D* **97** no. 12, (2018) 124058, [arXiv:1804.00660](#) [[gr-qc](#)].
- [29] W. Qin, K. K. Boddy, M. Kamionkowski, and L. Dai, “Pulsar-timing arrays, astrometry, and gravitational waves,” *Phys. Rev. D* **99** no. 6, (2019) 063002, [arXiv:1810.02369](#) [[astro-ph.CO](#)].
- [30] G. Mentasti and C. R. Contaldi, “Observing gravitational waves with solar system astrometry,” *JCAP* **05** (2024) 028, [arXiv:2311.03474](#) [[gr-qc](#)].
- [31] K. Inomata, M. Kamionkowski, C. M. Toral, and S. R. Taylor, “Overlap reduction functions for pulsar timing arrays and astrometry,” *Phys. Rev. D* **110** no. 6, (2024) 063547, [arXiv:2406.00096](#) [[astro-ph.CO](#)].
- [32] H. An, T. Li, J. Shu, X. Wang, X. Xue, and Y. Zhao, “Dark Photon Dark Matter and Low-Frequency Gravitational Wave Detection with Gaia-like Astrometry,” [arXiv:2407.16488](#) [[hep-ph](#)].
- [33] A. H. Jaffe, “Observing gravitational radiation with QSO proper motions and the SKA,” *New Astron. Rev.* **48** (2004) 1483–1485, [arXiv:astro-ph/0409637](#).
- [34] Z. Lu, L.-T. Wang, and H. Xiao, “A New Probe of μHz Gravitational Waves with FRB Timing,” [arXiv:2407.12920](#) [[gr-qc](#)].
- [35] L. Zwick, D. Soyuer, D. J. D’Orazio, D. O’Neill, A. Derdzinski, P. Saha, D. Blas, A. C. Jenkins, and L. Z. Kelley, “Bridging the micro-Hz gravitational wave gap via Doppler tracking with the Uranus Orbiter and Probe Mission: Massive black hole binaries, early universe signals and ultra-light dark matter,” [arXiv:2406.02306](#) [[astro-ph.HE](#)].
- [36] **Gaia** Collaboration, T. Prusti *et al.*, “The Gaia Mission,” *Astronomy and Astrophysics* **595** no. Gaia Data Release 1, (2016) A1, [arXiv:1609.04153](#) [[astro-ph.IM](#)].
- [37] A. Vallenari, A. G. A. Brown, *et al.*, “Gaia data release 3: Summary of the content and survey properties,” *Astronomy and Astrophysics* **674** (June, 2023) A1, [arXiv:2208.00211](#) [[astro-ph.GA](#)].
- [38] W. Schlüter and D. Behrend, “The International VLBI Service for Geodesy and Astrometry (IVS): current capabilities and future prospects,” *Journal of Geodesy* **81** no. 6-8, (June, 2007) 379–387.
- [39] O. Titov, S. B. Lambert, and A.-M. Gontier, “VLBI measurement of the secular aberration drift,” *Astronomy and Astrophysics* **529** (Apr., 2011) A91, [arXiv:1009.3698](#) [[astro-ph.CO](#)]. <http://dx.doi.org/10.1051/0004-6361/201015718>.
- [40] J. Darling, A. E. Truebenbach, and J. Paine, “Astrometric Limits on the Stochastic Gravitational Wave Background,” *Astrophys. J.* **861** no. 2, (2018) 113, [arXiv:1804.06986](#) [[astro-ph.IM](#)].
- [41] S. Aoyama, D. Yamauchi, M. Shiraishi, and M. Ouchi, “Gaia 400,894 QSO constraint on the energy density of low-frequency gravitational waves,” [arXiv:2105.04039](#) [[gr-qc](#)].
- [42] S. Jaraba, J. García-Bellido, S. Kuroyanagi, S. Ferraiuolo, and M. Braglia, “Stochastic gravitational wave background constraints from Gaia DR3 astrometry,” *Mon. Not. Roy. Astron. Soc.* **524** no. 3, (2023) 3609–3622, [arXiv:2304.06350](#) [[astro-ph.CO](#)].

- [43] J. Darling, “A new approach to the low frequency stochastic gravitational wave background: Constraints from quasars and the astrometric hellings-downs curve.” 2024. <https://arxiv.org/abs/2412.08605>.
- [44] R. E. Sanderson, A. Bellini, *et al.*, “Astrometry with the wide-field infrared space telescope.” 2019. <https://arxiv.org/abs/1712.05420>.
- [45] Y. Wang, K. Pardo, T.-C. Chang, and O. Doré, “Gravitational Wave Detection with Photometric Surveys,” *Phys. Rev. D* **103** no. 8, (2021) 084007, [arXiv:2010.02218](https://arxiv.org/abs/2010.02218) [gr-qc].
- [46] Y. Wang, K. Pardo, T.-C. Chang, and O. Doré, “Constraining the stochastic gravitational wave background with photometric surveys,” *Phys. Rev. D* **106** no. 8, (2022) 084006, [arXiv:2205.07962](https://arxiv.org/abs/2205.07962) [gr-qc].
- [47] K. Pardo, T.-C. Chang, O. Doré, and Y. Wang, “Gravitational Wave Detection with Relative Astrometry using Roman’s Galactic Bulge Time Domain Survey,” [arXiv:2306.14968](https://arxiv.org/abs/2306.14968) [astro-ph.GA].
- [48] **Theia** Collaboration, C. Boehm *et al.*, “Theia: Faint objects in motion or the new astrometry frontier,” [arXiv:1707.01348](https://arxiv.org/abs/1707.01348) [astro-ph.IM].
- [49] F. Malbet *et al.*, “Theia : science cases and mission profiles for high precision astrometry in the future,” in *SPIE Astronomical Telescopes + Instrumentation 2022*. 7, 2022. [arXiv:2207.12540](https://arxiv.org/abs/2207.12540) [astro-ph.IM].
- [50] J. Garcia-Bellido, H. Murayama, and G. White, “Exploring the early Universe with Gaia and Theia,” *JCAP* **12** no. 12, (2021) 023, [arXiv:2104.04778](https://arxiv.org/abs/2104.04778) [hep-ph].
- [51] V. Alba and J. Maldacena, “Primordial gravity wave background anisotropies,” *JHEP* **03** (2016) 115, [arXiv:1512.01531](https://arxiv.org/abs/1512.01531) [hep-th].
- [52] C. R. Contaldi, “Anisotropies of Gravitational Wave Backgrounds: A Line Of Sight Approach,” *Phys. Lett. B* **771** (2017) 9–12, [arXiv:1609.08168](https://arxiv.org/abs/1609.08168) [astro-ph.CO].
- [53] M. Geller, A. Hook, R. Sundrum, and Y. Tsai, “Primordial Anisotropies in the Gravitational Wave Background from Cosmological Phase Transitions,” *Phys. Rev. Lett.* **121** no. 20, (2018) 201303, [arXiv:1803.10780](https://arxiv.org/abs/1803.10780) [hep-ph].
- [54] N. Bartolo, D. Bertacca, S. Matarrese, M. Peloso, A. Ricciardone, A. Riotto, and G. Tasinato, “Anisotropies and non-Gaussianity of the Cosmological Gravitational Wave Background,” *Phys. Rev. D* **100** no. 12, (2019) 121501, [arXiv:1908.00527](https://arxiv.org/abs/1908.00527) [astro-ph.CO].
- [55] N. Bartolo, D. Bertacca, V. De Luca, G. Franciolini, S. Matarrese, M. Peloso, A. Ricciardone, A. Riotto, and G. Tasinato, “Gravitational wave anisotropies from primordial black holes,” *JCAP* **02** (2020) 028, [arXiv:1909.12619](https://arxiv.org/abs/1909.12619) [astro-ph.CO].
- [56] N. Bartolo, D. Bertacca, S. Matarrese, M. Peloso, A. Ricciardone, A. Riotto, and G. Tasinato, “Characterizing the cosmological gravitational wave background: Anisotropies and non-Gaussianity,” *Phys. Rev. D* **102** no. 2, (2020) 023527, [arXiv:1912.09433](https://arxiv.org/abs/1912.09433) [astro-ph.CO].
- [57] E. Dimastrogiovanni, M. Fasiello, A. Malhotra, P. D. Meerburg, and G. Orlando, “Testing the early universe with anisotropies of the gravitational wave background,” *JCAP* **02** no. 02, (2022) 040, [arXiv:2109.03077](https://arxiv.org/abs/2109.03077) [astro-ph.CO].
- [58] **LISA Cosmology Working Group** Collaboration, N. Bartolo *et al.*, “Probing anisotropies of the Stochastic Gravitational Wave Background with LISA,” *JCAP* **11** (2022) 009, [arXiv:2201.08782](https://arxiv.org/abs/2201.08782) [astro-ph.CO].
- [59] P. Adshead, N. Afshordi, E. Dimastrogiovanni, M. Fasiello, E. A. Lim, and G. Tasinato, “Multimessenger Cosmology: correlating CMB and SGWB measurements,” *Phys. Rev. D* **103** no. 2, (2021) 023532, [arXiv:2004.06619](https://arxiv.org/abs/2004.06619) [astro-ph.CO].

- [60] C. M. F. Mingarelli, T. Sidery, I. Mandel, and A. Vecchio, “Characterizing gravitational wave stochastic background anisotropy with pulsar timing arrays,” [*Phys. Rev. D* **88** no. 6, \(2013\) 062005](#), [arXiv:1306.5394 \[astro-ph.HE\]](#).
- [61] S. R. Taylor and J. R. Gair, “Searching For Anisotropic Gravitational-wave Backgrounds Using Pulsar Timing Arrays,” [*Phys. Rev. D* **88** \(2013\) 084001](#), [arXiv:1306.5395 \[gr-qc\]](#).
- [62] C. M. F. Mingarelli, T. J. W. Lazio, A. Sesana, J. E. Greene, J. A. Ellis, C.-P. Ma, S. Croft, S. Burke-Spolaor, and S. R. Taylor, “The local nanohertz gravitational-wave landscape from supermassive black hole binaries,” [*Nature Astronomy* **1** no. 12, \(Nov., 2017\) 886–892](#), [arXiv:1708.03491 \[astro-ph.GA\]](#).
- [63] S. R. Taylor, R. van Haasteren, and A. Sesana, “From Bright Binaries To Bumpy Backgrounds: Mapping Realistic Gravitational Wave Skies With Pulsar-Timing Arrays,” [*Phys. Rev. D* **102** no. 8, \(2020\) 084039](#), [arXiv:2006.04810 \[astro-ph.IM\]](#).
- [64] E. C. Gardiner, L. Z. Kelley, A.-M. Lemke, and A. Mitridate, “Beyond the Background: Gravitational-wave Anisotropy and Continuous Waves from Supermassive Black Hole Binaries,” [*Astrophys. J.* **965** no. 2, \(2024\) 164](#), [arXiv:2309.07227 \[astro-ph.HE\]](#).
- [65] G. Sato-Polito and M. Kamionkowski, “Exploring the spectrum of stochastic gravitational-wave anisotropies with pulsar timing arrays,” [*Phys. Rev. D* **109** no. 12, \(5, 2024\) 123544](#), [arXiv:2305.05690 \[astro-ph.CO\]](#).
- [66] **NANOGrav** Collaboration, G. Agazie et al., “The NANOGrav 15 yr Data Set: Search for Anisotropy in the Gravitational-wave Background,” [*Astrophys. J. Lett.* **956** no. 1, \(6, 2023\) L3](#), [arXiv:2306.16221 \[astro-ph.HE\]](#).
- [67] M. R. Sah, S. Mukherjee, V. Saeedzadeh, A. Babul, M. Tremmel, and T. R. Quinn, “Imprints of supermassive black hole evolution on the spectral and spatial anisotropy of nano-hertz stochastic gravitational-wave background,” [*Mon. Not. Roy. Astron. Soc.* **533** no. 2, \(2024\) 1568–1582](#), [arXiv:2404.14508 \[astro-ph.CO\]](#).
- [68] J. Raidal, J. Urrutia, V. Vaskonen, and H. Veermäe, “Statistics of the supermassive black hole gravitational wave background anisotropy,” [arXiv:2411.19692 \[astro-ph.CO\]](#).
- [69] G. Cusin and G. Tasinato, “Doppler boosting the stochastic gravitational wave background,” [*JCAP* **08** no. 08, \(2022\) 036](#), [arXiv:2201.10464 \[astro-ph.CO\]](#).
- [70] D. Chowdhury, G. Tasinato, and I. Zavala, “Response of the Einstein Telescope to Doppler anisotropies,” [*Phys. Rev. D* **107** no. 8, \(2023\) 083516](#), [arXiv:2209.05770 \[gr-qc\]](#).
- [71] G. Tasinato, “Kinematic anisotropies and pulsar timing arrays,” [*Phys. Rev. D* **108** no. 10, \(2023\) 103521](#), [arXiv:2309.00403 \[gr-qc\]](#).
- [72] D. Bertacca, A. Ricciardone, N. Bellomo, A. C. Jenkins, S. Matarrese, A. Raccanelli, T. Regimbau, and M. Sakellariadou, “Projection effects on the observed angular spectrum of the astrophysical stochastic gravitational wave background,” [*Phys. Rev. D* **101** no. 10, \(2020\) 103513](#), [arXiv:1909.11627 \[astro-ph.CO\]](#).
- [73] L. Valbusa Dall’Armi, A. Ricciardone, and D. Bertacca, “The dipole of the astrophysical gravitational-wave background,” [*JCAP* **11** \(2022\) 040](#), [arXiv:2206.02747 \[astro-ph.CO\]](#).
- [74] A. K.-W. Chung, A. C. Jenkins, J. D. Romano, and M. Sakellariadou, “Targeted search for the kinematic dipole of the gravitational-wave background,” [*Phys. Rev. D* **106** no. 8, \(2022\) 082005](#), [arXiv:2208.01330 \[gr-qc\]](#).
- [75] G. F. Smoot, M. V. Gorenstein, and R. A. Muller, “Detection of Anisotropy in the Cosmic Black Body Radiation,” [*Phys. Rev. Lett.* **39** \(1977\) 898](#).

- [76] A. Kogut *et al.*, “Dipole anisotropy in the COBE DMR first year sky maps,” [*Astrophys. J.* **419** \(1993\) 1](#), [arXiv:astro-ph/9312056](#).
- [77] **WMAP** Collaboration, C. L. Bennett *et al.*, “First year Wilkinson Microwave Anisotropy Probe (WMAP) observations: Preliminary maps and basic results,” [*Astrophys. J. Suppl.* **148** \(2003\) 1–27](#), [arXiv:astro-ph/0302207](#).
- [78] **Planck** Collaboration, N. Aghanim *et al.*, “Planck 2013 results. XXVII. Doppler boosting of the CMB: Eppur si muove,” [*Astron. Astrophys.* **571** \(2014\) A27](#), [arXiv:1303.5087 \[astro-ph.CO\]](#).
- [79] B. Allen and A. C. Ottewill, “Detection of anisotropies in the gravitational wave stochastic background,” [*Phys. Rev. D* **56** \(1997\) 545–563](#), [arXiv:gr-qc/9607068 \[gr-qc\]](#).
- [80] M. Anholm, S. Ballmer, J. D. E. Creighton, L. R. Price, and X. Siemens, “Optimal strategies for gravitational wave stochastic background searches in pulsar timing data,” [*Phys. Rev. D* **79** \(2009\) 084030](#), [arXiv:0809.0701 \[gr-qc\]](#).
- [81] J. Gair, J. D. Romano, S. Taylor, and C. M. F. Mingarelli, “Mapping gravitational-wave backgrounds using methods from CMB analysis: Application to pulsar timing arrays,” [*Phys. Rev. D* **90** no. 8, \(2014\) 082001](#), [arXiv:1406.4664 \[gr-qc\]](#).
- [82] S. C. Hotinli, M. Kamionkowski, and A. H. Jaffe, “The search for anisotropy in the gravitational-wave background with pulsar-timing arrays,” [*Open J. Astrophys.* **2** no. 1, \(2019\) 8](#), [arXiv:1904.05348 \[astro-ph.CO\]](#).
- [83] Y. Ali-Haïmoud, T. L. Smith, and C. M. F. Mingarelli, “Insights into searches for anisotropies in the nanohertz gravitational-wave background,” [*Phys. Rev. D* **103** no. 4, \(2021\) 042009](#), [arXiv:2010.13958 \[gr-qc\]](#).
- [84] Y. Ali-Haïmoud, T. L. Smith, and C. M. F. Mingarelli, “Fisher formalism for anisotropic gravitational-wave background searches with pulsar timing arrays,” [*Phys. Rev. D* **102** no. 12, \(2020\) 122005](#), [arXiv:2006.14570 \[gr-qc\]](#).
- [85] **LISA Cosmology Working Group** Collaboration, P. Auclair *et al.*, “Cosmology with the Laser Interferometer Space Antenna,” [*Living Rev. Rel.* **26** no. 1, \(4, 2022\) 5](#), [arXiv:2204.05434 \[astro-ph.CO\]](#).
- [86] N. J. Cornish and R. van Haasteren, “Mapping the nano-Hertz gravitational wave sky,” [arXiv:1406.4511 \[gr-qc\]](#).
- [87] S. R. Taylor *et al.*, “Limits on anisotropy in the nanohertz stochastic gravitational-wave background,” [*Phys. Rev. Lett.* **115** no. 4, \(2015\) 041101](#), [arXiv:1506.08817 \[astro-ph.HE\]](#).
- [88] P. F. Depta, V. Domcke, G. Franciolini, and M. Pironi, “Pulsar timing array sensitivity to anisotropies in the gravitational wave background,” [arXiv:2407.14460 \[astro-ph.CO\]](#).
- [89] T. Konstandin, A.-M. Lemke, A. Mitridate, and E. Perboni, “The impact of cosmic variance on PTAs anisotropy searches,” [arXiv:2408.07741 \[astro-ph.CO\]](#).
- [90] N. Pol, S. R. Taylor, and J. D. Romano, “Forecasting Pulsar Timing Array Sensitivity to Anisotropy in the Stochastic Gravitational Wave Background,” [*Astrophys. J.* **940** no. 2, \(2022\) 173](#), [arXiv:2206.09936 \[astro-ph.HE\]](#).
- [91] A.-M. Lemke, A. Mitridate, and K. A. Gersbach, “Detecting Gravitational Wave Anisotropies from Supermassive Black Hole Binaries,” [arXiv:2407.08705 \[astro-ph.HE\]](#).
- [92] R. C. Bernardo and K.-W. Ng, “Charting the Nanohertz Gravitational Wave Sky with Pulsar Timing Arrays,” [arXiv:2409.07955 \[astro-ph.CO\]](#).
- [93] M. Maggiore, [*Gravitational Waves. Vol. 2: Astrophysics and Cosmology*](#). Oxford University Press, 3, 2018.

- [94] M. Maggiore, [Gravitational Waves. Vol. 1: Theory and Experiments](#). Oxford University Press, 2007.
- [95] E. Roebber and G. Holder, “Harmonic space analysis of pulsar timing array redshift maps,” [Astrophys. J.](#) **835** no. 1, (2017) 21, [arXiv:1609.06758 \[astro-ph.CO\]](#).
- [96] J. Nay, K. K. Boddy, T. L. Smith, and C. M. F. Mingarelli, “Harmonic analysis for pulsar timing arrays,” [Phys. Rev. D](#) **110** no. 4, (2024) 044062, [arXiv:2306.06168 \[gr-qc\]](#).
- [97] M. Çalışkan, Y. Chen, L. Dai, N. Anil Kumar, I. Stomberg, and X. Xue, “Dissecting the stochastic gravitational wave background with astrometry,” [JCAP](#) **05** (2024) 030, [arXiv:2312.03069 \[gr-qc\]](#).
- [98] F. A. Jenet and J. D. Romano, “Understanding the gravitational-wave Hellings and Downs curve for pulsar timing arrays in terms of sound and electromagnetic waves,” [Am. J. Phys.](#) **83** (2015) 635, [arXiv:1412.1142 \[gr-qc\]](#).
- [99] M. Tegmark, “How to measure CMB power spectra without losing information,” [Phys. Rev. D](#) **55** (1997) 5895–5907, [arXiv:astro-ph/9611174](#).
- [100] D. Alonso, C. R. Contaldi, G. Cusin, P. G. Ferreira, and A. I. Renzini, “Noise angular power spectrum of gravitational wave background experiments,” [Phys. Rev. D](#) **101** no. 12, (2020) 124048, [arXiv:2005.03001 \[astro-ph.CO\]](#).
- [101] N. M. J. Cruz, A. Malhotra, G. Tasinato, and I. Zavala, “Measuring kinematic anisotropies with pulsar timing arrays,” [Phys. Rev. D](#) **110** no. 6, (2024) 063526, [arXiv:2402.17312 \[gr-qc\]](#).
- [102] N. M. J. Cruz, A. Malhotra, G. Tasinato, and I. Zavala, “Measuring the circular polarization of gravitational waves with pulsar timing arrays,” [Phys. Rev. D](#) **110** no. 10, (2024) 103505, [arXiv:2406.04957 \[astro-ph.CO\]](#).
- [103] A. Heavens, “Statistical techniques in cosmology,” (2009) , [arXiv:0906.0664 \[astro-ph.CO\]](#).
- [104] T.-T. Lu and S.-H. Shiou, “Inverses of 2×2 block matrices,” [Computers and Mathematics with Applications](#) **43** no. 1-2, (2002) 119–129.
- [105] R. A. Horn and C. R. Johnson, [Matrix analysis](#). Cambridge university press, 2012.
- [106] A. Lewis, “GetDist: a Python package for analysing Monte Carlo samples,” [arXiv:1910.13970 \[astro-ph.IM\]](#).